



Enhanced peroxyomonosulfate activation by S-scheme AgI/Cu-BiVO₄ heterojunction for efficient photocatalytic organics degradation and *Microcystis aeruginosa* inactivation: Performance, interfacial engineering and mechanism insight

Jing Li ^a, Dandan Wang ^a, Siyuan Zhao ^a, Rui Ma ^a, Jifeng Guo ^{a,*}, Zhuoya Li ^a, Dong Wang ^b, Yue Xuan ^b, Liping Wang ^{c,*}

^a Key Laboratory of Subsurface Hydrology and Ecological Effects in Arid Region of the Ministry of Education, Key Laboratory of Eco-hydrology and Water Security in Arid and Semi-arid Regions of Ministry of Water Resources, School of Water and Environment, Chang'an University, Xi'an 710054, PR China

^b School of Energy and Power Engineering, Shandong University, Jinan, Shandong 250061, PR China

^c College of Geology and Environment, Xi'an University of Science and Technology, Xi'an 710054, PR China



ARTICLE INFO

Keywords:

AgI/Cu-BiVO₄
Interface engineering
S-scheme heterojunction
Peroxyomonosulfate
Photocatalytic degradation

ABSTRACT

Novel oxygen vacancies-enriched AgI/Cu-BiVO₄ (ACBV) S-scheme heterojunction catalysts were constructed to boost photocatalytic organics degradation and *M. aeruginosa* inactivation with peroxyomonosulfate (PMS) assistance. Specific interfacial charge transfer and abundant active centers were guided by introducing Cu doping and AgI coupling into BiVO₄, with the catalytic activity and mechanism systematically investigated. The optimal 0.25-ACBV heterojunction exhibited 97.6% tetracycline (TC) degradation under PMS-assisted visible light and achieved effective inactivation of *M. aeruginosa* within 20 min (78.8%). The S-scheme heterostructure from Cu-BiVO₄ to AgI and synergistic effects endowed the system with high-energy carrier transfer kinetics and strong oxygen reduction capability. Meanwhile, the redox cycling of Cu²⁺/Cu⁺ and surface oxygen defects served as electron acceptors to accelerate interfacial charge separation and as adsorption activation sites for PMS, promoting efficient mass transfer in the non-homogeneous system. This study inspires the design of high-performance S-scheme photocatalytic activators and expands their potential applications in environmental remediation.

1. Introduction

Sustainable energy production and water pollution control have emerged as pivotal areas of global research. Organic pollutants, such as antibiotics and algal organisms, are widely present in natural water bodies. Among them, tetracycline (TC) antibiotics, characterized by their broad-spectrum, high efficiency, and low-cost properties, have been extensively employed in the fields of human medicine, aquaculture, and animal husbandry [1]. However, TC contamination leads to an increased risk of antibiotic-resistant bacteria in water bodies and disrupts aquatic ecosystems [2,3]. Simultaneously, algal growth can potentially cause issues such as harmful algal blooms (HABs), algal toxin production, and water-body odor [4,5]. Recent studies reported that antibiotic pollutants and cyanobacteria coexist in natural water bodies,

and low-concentration antibiotics may promote the growth of *Microcystis aeruginosa* (*M. aeruginosa*), thereby exacerbating bloom formation and the accumulation of algal toxins [6,7]. Therefore, it is crucial to develop integrated water treatment strategies to degrade antibiotics, inactivate algal growth and improve water quality. Visible-light-driven photocatalytic technology, with advantages such as low energy consumption, non-selective mineralization, and mild reaction conditions, holds great potential in organic pollutant removal and HABs control [8–10].

Among the visible-light-driven Bi-based photocatalysts, bismuth vanadate (BiVO₄) receives widespread attention for its suitable band gap (2.4 eV), non-toxicity, excellent visible-light responsiveness, and chemical stability [11]. However, the inherent defects of BiVO₄, such as low conduction band potential (+0.3–0.4 eV) and high charge

* Correspondence to: School of Water and Environment, Chang'an University, Xi'an 710054, PR China.

E-mail addresses: guojifeng@chd.edu.cn (J. Guo), lipingwang@xust.edu.cn (L. Wang).



Scheme 1. Schematic diagram of AgI/Cu-BiVO₄ composites preparation process.

recombination rate, limit its practical application in photocatalysis [12, 13]. The construction of heterojunctions was regarded as an ideal strategy to modulate internal charge transport and overcome carrier recombination in single-phase BiVO₄ [14]. Moreover, the formation of heterojunction phase interfaces often induces lattice mismatches and distortions, leading to the formation of vacancies [15]. Recently proposed step-scheme (S-scheme) heterojunctions offer unique advantages in facilitating charge separation [16]. Driven by the built-in electric field (BIEF), band bending and Coulomb force at the interface, the low-energy holes in the reduced photocatalyst (RP) and the electrons in the oxidized photocatalyst (OP) accelerate the combination, which cleverly achieves the dual modulation of strong redox capability and efficient carrier separation [17]. Therefore, the construction of S-scheme heterojunctions using BiVO₄ with typical OP properties has been proven to be an effective strategy for modulating carrier transport pathways and enhancing photocatalytic performance, such as BiVO₄/CsPbBr₃ [14], BiVO₄/g-C₃N₄ [18], B-TiO₂/BiVO₄ [9], and Ni-MOF-74/BiVO₄ [11]. Inspired by this, silver iodide (AgI), as a typical photosensitive silver halide with excellent visible light absorption and reducing properties [19], has found extensive applications in the inactivation of bacteria and microalgae as well as in the degradation of organic substances [20,21]. More importantly, AgI has a higher E_f and an energy band structure matching with BiVO₄. The electronic configuration of BiVO₄ can be tuned by utilizing AgI as an electron donor to construct S-scheme heterojunctions with optimal interfacial effects [22,23]. This coupling promotes accelerated charge separation and transfer while preserving the powerful reducing electrons of AgI and the high oxidation holes of BiVO₄ [17]. Although the enhancement of carrier separation kinetics is achieved through heterostructure, the single photocatalytic technique still has limitations in the mineralization of refractory organic pollutants [12].

Recently, peroxyomonosulfate (PMS) activation-assisted photocatalytic systems based on advanced oxidation processes (AOPs) have been considered effective approaches for rapidly achieving pollutant removal [24]. Under visible light irradiation, PMS can act as an electron acceptor to facilitate the separation and transfer of photoexcited carriers [25]. Simultaneously, the carriers can activate the O-O bonds in the asymmetric configuration of PMS molecules to generate sulfate radicals (SO₄^{·-}) with higher redox potentials (E⁰=2.5–3.1 eV), a longer half-life (30–40 μs), and more extensive pH adaptability [15]. We anticipate

that the modification of BiVO₄ with AgI to construct S-scheme heterojunction could achieve synergistic effects in PMS-activated photocatalysis, thus efficiently mineralizing pollutants [13,26]. Moreover, it addresses the issues of power consumption and metal leaching inherent in traditional Fenton technology [12]. Therefore, the rational improvement of the heterojunction to enhance the effective mass transfer between the catalyst and PMS is a critical step to promote ROS generation and achieve high activity for pollutant removal.

Considering the induced effect of transition metal ions (Fe³⁺, Al³⁺ and Cu²⁺) on surface oxygen vacancies, doping transition metal ions in heterojunctions can achieve dual modulation of accelerated carrier transfer kinetics and PMS activation [27,28]. Particularly, Cu²⁺ serves as an interesting dopant/activator with low-cost, plasmonic and antibacterial properties. It induces favorable conditions on the BiVO₄ energy band by optimizing interfacial contacts, electronic structure and induced defect energy levels [29]. The hybridization bands and surface oxygen vacancies formed by Cu²⁺ doping can modulate the local coordination environment and lower the energy level jump barriers, thus expanding the light absorption range of BiVO₄ [30,31]. Moreover, it promotes carrier rearrangement and interfacial charge transfer by utilizing the distinctive Cu²⁺/Cu⁺ redox cycling and oxygen defects as electron traps, while effectively inhibiting the leaching of copper ions [32]. Also, they act as active sites for PMS activation, promoting efficient mass transfer in the non-homogeneous phase [33]. The Cu²⁺ ions are easily doped into the BiVO₄ lattice due to their smaller radius (0.72 Å) compared to Bi³⁺ (1.17 Å) [34]. Previous investigations reported the positive inhibitory effect of Cu²⁺ ions on the growth of *M. aeruginosa* during photocatalysis [35]. It is speculated that the construction of S-scheme AgI/Cu-BiVO₄ heterojunctions doped with Cu²⁺ by controlling the Cu doping amount and optimizing the synthesis conditions using surface modifiers. This will accelerate PMS activation and induce rapid charge transfer, thus achieving the dual effects of efficient pollutant mineralization and algae inactivation. However, there are no studies on the synergistic effects of charge transfer and PMS activation on antibiotic degradation in AgI/Cu-BiVO₄ S-scheme heterojunctions. Additionally, the activation of PMS by AgI/Cu-BiVO₄ catalyst to inactivate *M. aeruginosa* under visible light conditions has not been reported. Therefore, we prioritize research on the AgI/Cu-BiVO₄ heterojunction for PMS-activated photocatalytic degradation of antibiotics and inhibition of HABs.

Herein, this study aimed to rationally construct an S-scheme AgI/Cu-BiVO₄ (ACBV) heterojunction to achieve the dual modulation of photocarrier directional migration and PMS activation sites. The optimization of the electronic structure of the heterojunction by AgI and Cu²⁺ facilitated enhanced interfacial contact and oxygen defects generation, consequently resulting in enhanced visible light absorption and PMS activation. The heterojunction exhibited efficient degradation of TC and rapid inactivation of *M. aeruginosa* by PMS activation-assisted photocatalysis. The electronic configuration, internal electron transfer, and ROS transition were analyzed experimentally and theoretically by *in-situ* synchrotron illumination XPS (In-situ XPS), density functional theory (DFT) calculations and electron paramagnetic resonance (EPR). The S-scheme interfacial migration provided direct evidence for the rearrangement and selective accumulation of the electron-rich (AgI) and electron-poor (Cu-BiVO₄) regions in the heterojunction. Additionally, the activation mechanism of Cu²⁺/Cu⁺ redox cycling and oxygen vacancies as electron traps and PMS adsorption sites in AgI/Cu-BiVO₄ was revealed. This unique structure compensated for charge balance, enhanced PMS adsorption on its surface, and promoted high-energy electron transfer to PMS, thereby achieving efficient mass transfer. This study holds potential applications in organic pollutant mineralization and HABs water purification.

2. Experimental

2.1. Reagents

Bismuth nitrate pentahydrate (Bi(NO₃)₃·5 H₂O), ammonium metavanadate (NH₄VO₃), silver nitrate (AgNO₃), potassium peroxonosulfate (PMS, 2KHSO₅·KHSO₄·K₂SO₄), tetracycline (TC), oxytetracycline (OTC), norfloxacin (NOR), methylene Blue (MB), Rhodamine B (RhB), humic acid (HA), benzoic acid (BA) and nitrobenzene (NB) were purchased from Aladdin Chemical Reagents Co. Ltd. Potassium iodide (KI), copper nitrate trihydrate (Cu(NO₃)₂·3 H₂O), disodium ethylenediamine tetraacetate (EDTA-2Na), p-benzoquinone (BQ), sodium dodecyl sulfate (SDS, C₁₂H₂₅SO₄Na), tert-butanol (TBA), ammonium oxalate (AO), L-histidine, furfuryl alcohol (FFA), β-carotene and methanol (MeOH) were purchased from Sinopharm Chemical Reagent Co. Ltd. All reagents in this study were analytically pure, and the aqueous solution was deionized water.

2.2. Catalysts preparation

AgI/Cu-BiVO₄ (ACBV) composites were synthesized by a two-step method (Scheme 1). Firstly, the modified Cu-doped BiVO₄ (Cu-BiVO₄) catalyst was prepared by the surfactant-assisted hydrothermal method. Briefly, 5 mmol of Bi(NO₃)₃·5 H₂O and 5 mmol of NH₄VO₃ were completely dissolved in deionized water, respectively. Then, 1 g of SDS and 0.5 mmol Cu(NO₃)₂·3 H₂O were dissolved into the above mixture and stirred vigorously for 30 min. The mixture was finally transferred to a Teflon-lined autoclave and hydrothermally reacted at 140 °C for 20 h. After natural cooling, sufficient washing with water and ethanol, and vacuum drying, the yellow Cu-BiVO₄ catalyst was obtained. The AgI/Cu-BiVO₄ composites were synthesized through the *in-situ* chemical deposition method. Specifically, a certain amount of Cu-BiVO₄ was dispersed into an aqueous AgNO₃ solution with a theoretical molar ratio of 0.25, followed by 30 min of consecutive ultrasonic treatment to form a suspension. Subsequently, an aqueous solution of KI with the same molar ratio as AgNO₃ was added under dark conditions with vigorous stirring for 5 h. The resulting product was collected by filtration and washed thoroughly with water and ethanol, and dried overnight at 60 °C to obtain the 0.25-ACBV catalyst. Under the same conditions, x-ACBV catalysts with different AgI deposition were prepared by adjusting the addition amounts of AgNO₃ and KI (x=0.2, 0.25, 0.33, 0.5). In addition, for comparison, pure BiVO₄ and pure AgI were obtained by a similar method without the addition of Cu(NO₃)₂·3 H₂O and Cu-BiVO₄.

2.3. Characterization

The crystal structure of the samples was measured by X-ray diffraction (XRD, Bruker D8-advance, Germany) with Cu-K α irradiation ($\lambda = 0.154$ nm) in the range of 5–80°. Fourier transform infrared spectroscopy (FT-IR, PerkinElmer, USA) was used to analyze the functional groups of the samples. The microscopic morphology, lattice information, and elemental distribution of the catalysts were investigated using scanning electron microscopy (SEM, Hitachi S-4800, Japan) and transmission electron microscopy (TEM, JEM 2100 F, Japan). The chemical valence states of surface elements were characterized using X-ray photoelectron spectroscopy (XPS, Thermo Scientific ESCALAB Xi+, USA). Raman spectra were recorded using a Raman spectrometer (HORIBA HR Evolution) with a YAG solid-state exciter at 532 nm. *In-situ* synchronous illumination XPS spectra (In-situ XPS) was performed on an ESCALAB 250Xi (USA). Material surface potential was measured in Malvern Zetasizer (Nano ZEN3700, UK). Fluorescent organic components were measured by fluorescence spectrophotometer (3D EEM, F-7100, Shimadzu, Japan) with scanning parameters of excitation wavelengths of 200–450 nm, emission wavelengths of 250–550 nm, a slit width of 10 nm, and a step size of 5 nm. The UV-vis diffuse reflectance spectra (UV-vis -DRS) were recorded using UV-vis diffuse reflectance spectroscopy (TU-1901, Japan) with BaSO₄ as the reference standard. The photoluminescence spectra (PL) were measured at room temperature using transient fluorescence spectrometer (HORIBA Fluorolog-QM, Canada) with an excitation wavelength of 425 nm. Temperature-programmed desorption (TPD) of adsorption O₂ from samples was recorded using BSD-Chem C200.

2.4. Photocatalytic degradation measurement and analytical methods

The photochemical reactor (CEL-LAX500) equipped with the 300 W xenon lamp ($\lambda > 420$ nm) was used to continuously simulate the visible light source for PMS-activated photocatalytic degradation experiments. Typically, 30 mg of as-prepared catalyst was dispersed in 50 mL of TC solution (20 mg/L) and stirred continuously for 30 min in dark conditions to reach the adsorption-desorption equilibrium. Next, PMS (1.0 mM) was rapidly added to the reaction system and the light source was turned on for the photocatalytic reaction. At predetermined time intervals, 3 mL of the suspension was collected and quenched with 0.2 mL of methanol. The suspension was filtered through a 0.45 μ m filter membrane, and then the absorbance of the filtrate was measured at 356 nm using a UV-visible spectrophotometer (Shimadzu UV-3600) to analyze the concentration of TC. The total organic carbon (TOC) analyzer (TOC-V CPH, Shimadzu, Japan) and COD detector (5B-3 F (V10), China) were employed to evaluate the mineralization performance of the catalytic process. Details of the batch experiments, photoelectrochemical measurements, active species and TC degradation intermediates detection are listed in Text S1.

2.5. Evaluation of optical properties of photocatalysts

The six-flux model (SFM) was applied to determine the local volumetric rate of photon absorption (LVRPA) for the catalysts in the reactor, providing an in-depth study of the effects of the optical parameters of the catalyst (absorption and scattering coefficients), the optical thickness of the reactor (τ_{app}) and the total rate of photon absorption (TRPA) on the photocatalytic efficiency [36,37].

$$k^* = \frac{\int_{\lambda_{min}}^{\lambda_{max}} k_{\lambda}^* I_{\lambda} d\lambda}{\int_{\lambda_{min}}^{\lambda_{max}} I_{\lambda} d\lambda} \quad (1)$$

$$\sigma^* = \frac{\int_{\lambda_{min}}^{\lambda_{max}} \sigma_{\lambda}^* I_{\lambda} d\lambda}{\int_{\lambda_{min}}^{\lambda_{max}} I_{\lambda} d\lambda} \quad (2)$$

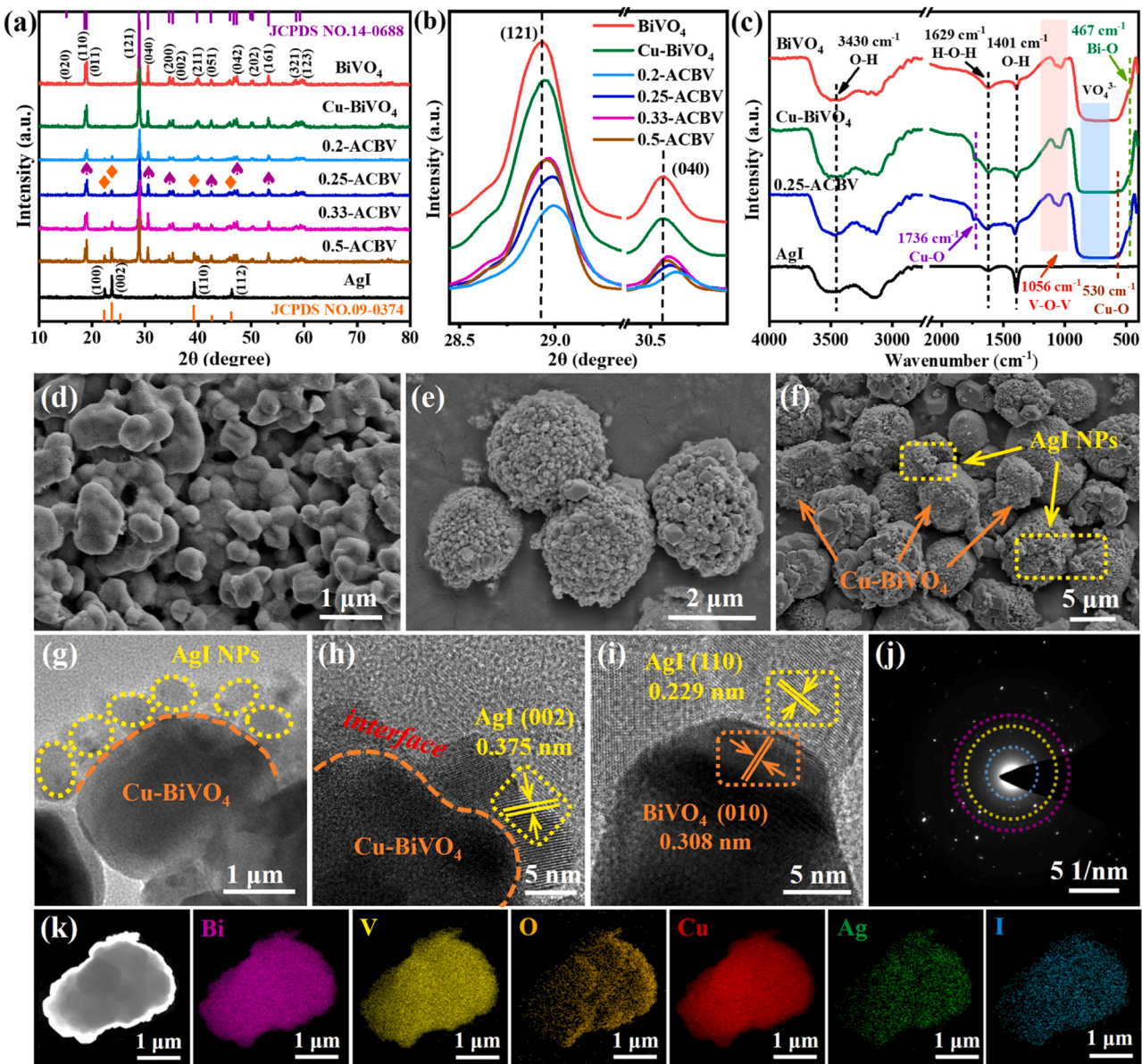


Fig. 1. (a) XRD spectra, (b) locally enlarged XRD spectra and (c) FT-IR spectra of AgI, BiVO₄, Cu-BiVO₄ and ACBV composites. SEM images of (d) AgI, (e) BiVO₄, (f) 0.25-ACBV; (g) TEM, (h, i) HRTEM, (j) SAED pattern and (k) EDX images of 0.25-ACBV.

$$\tau = (\sigma^* + k^*) C_{cat} L \quad (3)$$

$$\beta^* = \sigma^* + k^* \quad (4)$$

where β^* , σ^* , and k^* are the photocatalyst-specific extinction, scattering, and absorption coefficients (m^2/kg), and C_{cat} and L are the catalyst concentration (g/L) and the solution depth (m) within the flat reactor [38,39]. In this experimental reactor, C_{cat} was 0.2–1.0 g/L and L was 0.01 m.

The apparent optical thickness (τ_{app}) is:

$$\tau_{app} = a\tau \sqrt{1 - \omega_{corr}^2} \quad (5)$$

Eqs. (6–10) are used to quantify the LVRPA.

$$\text{LVRPA} = \frac{I_0 \tau_{app}}{\omega_{corr}(1 - \gamma)L} [\omega_{corr} - 1 + \sqrt{1 - \omega_{corr}^2} e^{-\frac{\pi \tau_{app}}{L}} + \gamma(\omega_{corr} - 1 - \sqrt{1 - \omega_{corr}^2} e^{\frac{\pi \tau_{app}}{L}})] \quad (6)$$

$$a = 1 - \omega p_f - \frac{4\omega^2 p_s^2}{1 - \omega p_f - \omega p_b - 2\omega p_s} \quad (7)$$

$$b = \omega p_b + \frac{4\omega^2 p_s^2}{1 - \omega p_f - \omega p_b - 2\omega p_s} \quad (8)$$

$$\omega_{corr} = \frac{b}{a} \quad (9)$$

$$\gamma = \frac{1 - \sqrt{1 - \omega_{corr}^2}}{1 + \sqrt{1 - \omega_{corr}^2}} e^{-2\tau_{app}} \quad (10)$$

Where p_b , p_f , and p_s represent backward, forward, and sideward scattering probabilities, respectively, as determined by the Henyey-Greenstein phase function for each photocatalyst [40] [41].

The TRPA represents the overall radiation absorbed within the entire reactor volume and serves as a useful parameter for determining the photoreactor efficiency and the optimal photocatalyst concentration for operating the photoreactor [41,42].

The TRPA per unit surface area is:

$$TRPA / A = \int_0^L LVRPA \, dx \quad (11)$$

2.6. Photocatalytic inactivation of *M. aeruginosa*

The PMS-assisted photocatalytic inactivation of *M. aeruginosa* (No. FACHB 315) was performed in the specific photochemical reactor (CEL-LAX500), with an initial algae density of 5.0×10^6 cells/mL, close to the typical algae density for HABs occurring in natural waters. The PMS-activated photocatalytic performance of the samples was assessed by the inactivation of *M. aeruginosa*. The cultivation and measurement methods of *M. aeruginosa* are detailed in Text S2. All experiments were repeated three times and the mean values were reported.

2.7. Theoretical calculations

Density Functional Theory (DFT) calculations were performed based on Materials Studio 8.0 software and CASTEP module. The generalized gradient approximation (GGA) of the Perdew-Burke-Ernzerhof (PBE) function was employed to describe the exchange-correlation potential [43,44]. In all calculations, the cut-off energy of the plane-wave basis set was 550 eV, and the convergence criteria for total energy and Hellmann-Feynman forces were set to 10^{-5} eV and 0.02 eV/Å. The Cu-BiVO₄ bulk model was constructed by substituting Cu at the Bi site based on experimental concentrations. The Monkhorst-Pack k-point grid was set to $6 \times 6 \times 3$ for BiVO₄ and Cu-BiVO₄, and $2 \times 2 \times 1$ for AgI, for geometry optimization and electronic structure calculations. The crystal surfaces of BiVO₄ (010), Cu-BiVO₄ (010), and AgI (002) were selected and optimized for the calculation of the work function and the charge density difference. The adsorption energy (E_{ads}) was calculated as $E_{ads} = E_{Total} - E_{substrate} - E_{PMS}$, where E_{Total} , $E_{substrate}$, and E_{PMS} represent the total energy of the catalyst with PMS, catalysts, and PMS molecule, respectively [45]. A vacuum of 20 Å was used to eliminate the interactions between periodic structures in the structural relaxation process.

The molecular structure optimization and wave function analysis of TC was calculated by Gaussian 09 program with B3LYP/6-311 G* [46]. The Hirshfeld charge and Fukui index of TC were obtained by Multiwin 3.8. The VMD 1.9.4 procedure was applied to map the electrostatic potential (ESP) and isosurfaces of the Fukui index mapping.

The Fukui function could be depicted as follows [26,47]:

$$f(r) = \left[\frac{\partial \rho(r)}{\partial N} \right]_{V(r)} \quad (12)$$

$$\text{Nucleophilic attack : } f^+(r) = q_{N+1}(r) - q_N(r) \quad (13)$$

$$\text{Electrophilic attack : } f^-(r) = q_N(r) - q_{N-1}(r) \quad (14)$$

$$\text{Radical attack : } f^0(r) = \frac{f^+(r) + f^-(r)}{2} = \frac{q_{N+1}(r) - q_N(r)}{2} \quad (15)$$

Where $q(r)$, N , and v are respectively the electron density at a point r , the total number of electrons, and the external potential constant.

3. Results and discussion

3.1. Characterization

3.1.1. Structure and morphology

The crystal structure of the series catalysts was characterized by XRD. As shown in Fig. 1a, the pristine AgI was indexed as hexagonal β-AgI (JCPDS No. 09-0374) [20]. BiVO₄ prepared by the SDS-assisted hydrothermal method matched the monoclinic phase of BiVO₄ (JCPDS No. 14-0688) [4]. In the Cu/BiVO₄ sample, the doping of Cu does not

alter the phase structure of monoclinic BiVO₄, which may be due to the doping of Cu ions into the BiVO₄ lattice [34]. The coexistence of AgI and Cu-BiVO₄, confirming their successful assembly. Interestingly, the diffraction peak (121) of Cu-BiVO₄ shifts to a higher angle compared with pristine BiVO₄ (Fig. 1b). This shift may be attributed to the disorder of the Cu positions within the lattice and the doping substitution of Cu²⁺ (0.72 Å) for Bi³⁺ (1.17 Å), leading to a reduction in the interplanar spacing of BiVO₄ [29]. Notably, in ACBV composites, the characteristic peak intensities of AgI (002) and (110) crystal planes gradually increase with the addition of AgI content. In contrast, the intensities of (121) and (040) crystal faces of Cu-BiVO₄ exhibit an increasing-decreasing trend. This phenomenon may be related to the compressive stress generated by AgI embedment. The introduction of moderate amount of AgI is expected to improve the Cu-BiVO₄ lattice structure and lead to lattice contraction, which promotes the interlayer migration of photoexcited carriers. Nevertheless, as the AgI proportion continues to rise, excessive AgI deposition competes with the Cu-BiVO₄ lattice, disrupting the orderliness of the Cu-BiVO₄ lattice, consequently resulting in a reduction in the peak intensities for the (121) and (040) crystal planes [26,48].

The FT-IR spectra of the catalysts were further investigated (Fig. 1c). Apparently, the characteristic spectra at 3430, 1629 and 1401 cm⁻¹ for all samples arise from the asymmetric stretching vibrations of the H-O-H and O-H bonds of surface adsorbed water [49]. Due to the high transparency of AgI in the mid-infrared region, no significant absorption peaks of AgI were observed [50]. For BiVO₄ and Cu-BiVO₄, the absorption peaks at 467 and 1056 cm⁻¹ corresponded to Bi-O and V-O-V bond stretching vibrations, respectively [51]. While the absorption bands in 620–820 cm⁻¹ were related to VO₄³⁻ and V-O bond stretching vibrations [52]. Additionally, weak peaks of Cu-BiVO₄ at 530 and 1736 cm⁻¹ indicated the incorporation of Cu²⁺ into the BiVO₄ lattice as this is attributed to the Cu-O stretching vibrations [51]. The 0.25-ACBV composites exhibited similar infrared absorption characteristics as Cu-BiVO₄. Notably, the VO₄³⁻ vibration band was slightly redshifted due to the obvious interfacial interaction caused by AgI embedding into the lattice structure of Cu-BiVO₄ [48].

The surface morphology and microstructure were analyzed by SEM, TEM and HRTEM. Pristine AgI nanoparticles with diameters of approximately 300–500 nm were observed (Fig. 1d). Pristine BiVO₄ shows microspheres assembled by numerous nanoparticles, with a diameter of 3 μm and the presence of few intermediate polyhedra, probably due to the different growth stages and the self-assembly effect of SDS as surfactant (Fig. 1e) [53]. Cu-BiVO₄ exhibits slight agglomeration with a rough surface (Fig. S1a), indicating Cu²⁺ doping promotes the growth and aggregation of BiVO₄ crystals [34], thereby providing more adsorption and reaction active sites for subsequent catalytic reactions. The SEM image of the 0.25-ACBV sample reveals the deposition of AgI nanoparticles on the surface of Cu-BiVO₄ microspheres (Fig. 1f). The loading of AgI nanoparticles on the surface of the 0.33-ACBV sample increased with increasing AgI loading (Fig. S1b), and significant AgI deposition was observed in 0.5-ACBV (Fig. S1c). Additionally, the TEM image of 0.25-ACBV (Fig. 1g) further confirms that AgI nanoparticles are uniformly anchored on the exterior of Cu-BiVO₄ microspheres. The HRTEM images (Fig. 1h-i) further verify the closely interacting interface. The (002) crystal plane (0.375 nm) [54] and (110) crystal plane (0.229 nm) [20] of AgI were clearly located around the (121) crystal plane (0.308 nm) [49] of monoclinic BiVO₄. These results indicate that the AgI/Cu-BiVO₄ heterojunction with interacting interface was successfully constructed via a simple in-situ chemical deposition method. Notably, the selected area electron diffraction (SAED) pattern with different diffraction rings illustrates the polycrystalline structure and multi-component character of the 0.25-ACBV heterojunction (Fig. 1j). Additionally, the EDX elemental maps corresponding to Bi, V, Cu, O, Ag and I fully validated the well-grown AgI/Cu-BiVO₄ heterojunction catalyst (Fig. 1k).

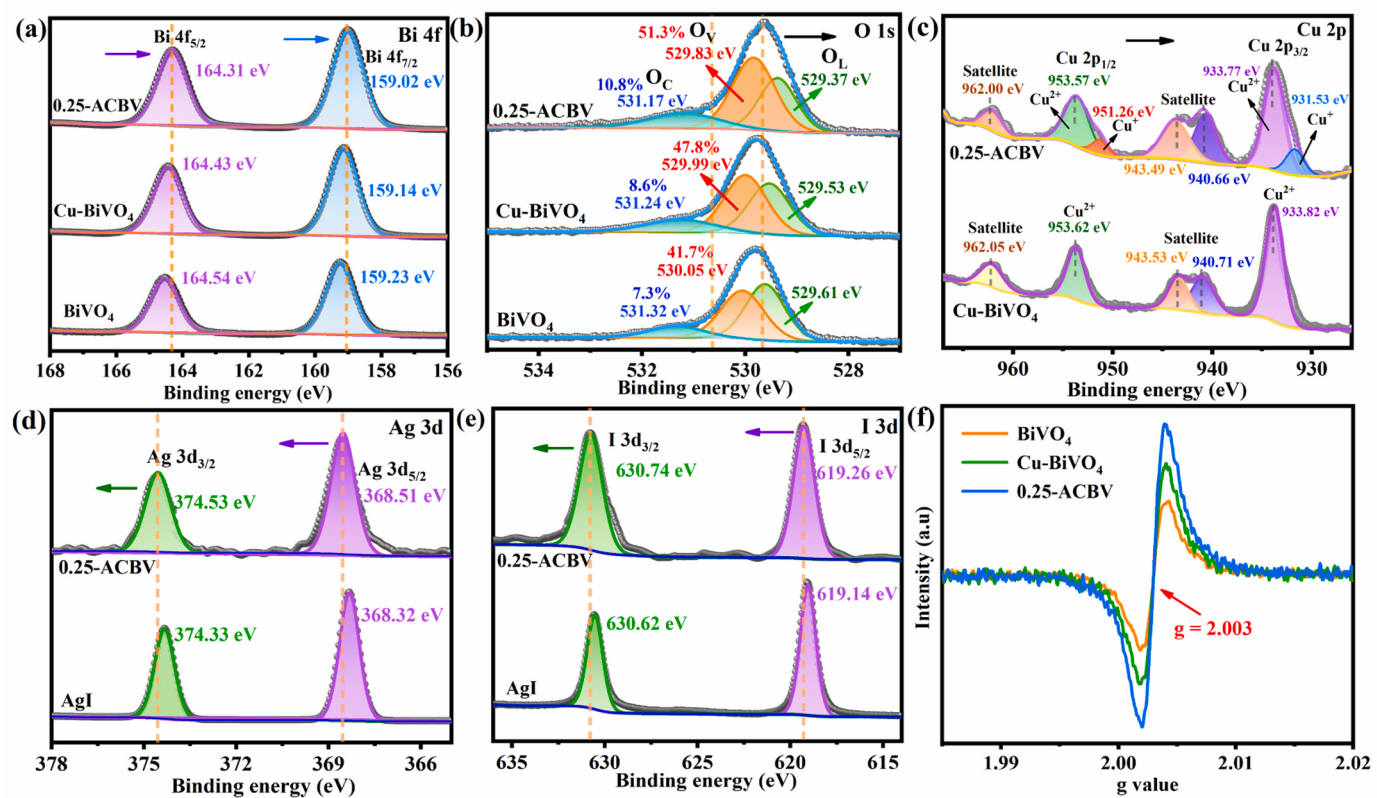


Fig. 2. XPS spectra of (a) Bi 4 f, (b) O 1 s of BiVO₄, Cu-BiVO₄ and 0.25-ACBV, (c) Cu 2p of Cu-BiVO₄ and 0.25-ACBV, (d) Ag 3d, (e) I 3d of AgI and 0.25-ACBV. (f) EPR spectra of BiVO₄, Cu-BiVO₄ and 0.25-ACBV.

3.1.2. Surface chemical properties

The chemical behavior of the catalyst surface elements was determined by XPS. The XPS survey spectra (Fig. S2a-b) and surface elemental content proportions (Fig. S2c) of the catalyst confirmed the well coupling of AgI and Cu-BiVO₄ in the heterojunction. The Bi 4 f spectra of 0.25-ACBV at 164.31 and 159.02 eV correlate with Bi³⁺ of Bi 4 f_{5/2} and Bi 4 f_{7/2}, respectively (Fig. 2a) [11]. It was observed that the Bi 4 f peak in the 0.25-ACBV heterojunction shifted to a low binding energy position (0.2 eV), which indicates an increase in electron density [55]. Additionally, a similar negative shift was observed in the V 2p spectra (Fig. S2d), suggesting that this interfacial electron push-pull effect promotes charge transfer [26]. The spectra of O 1 s in Fig. 2b could be fitted to lattice oxygen (O_L), metal cation-associated surface oxygen vacancies (O_V), and oxygen chemisorbed (O_C) [30]. Apparently, the contribution of O_V increased from 41.7% (BiVO₄) to 47.8% (Cu-BiVO₄) and 51.3% (0.25-ACBV) (Table S1 and Fig. S2e). This indicates that the construction of 0.25-ACBV heterojunction successfully induced more oxygen defects, which reduced the band gap and enhances the absorption of visible light. OVs could act as electron traps, accelerating charge transfer and prolonging carrier lifetimes, resulting in improved PMS activation and photocatalytic reaction rates [29]. Additionally, OVs act as specific active sites to convert adsorbed oxygen and PMS on the catalyst surface into reactive oxygen species to realize the degradation of pollutants [12,34]. The chemisorbed water content on the surface of 0.25-ACBV (10.8%) was higher than that of BiVO₄ (7.3%) and Cu-BiVO₄ (8.6%), which suggested that the heterojunction enhanced the concentration of surface-adsorbed H₂O and -OH groups on the catalyst surface. The surface-adsorbed -OH groups exhibited a synergistic effect on PMS activation and ROS production, promoting the O-O bond cleavage of PMS and the subsequent generation of ROS species. As displayed in Fig. 2c, the characteristic peaks of Cu-BiVO₄ at 933.82 and 953.62 eV could be attributed to the Cu 2p_{3/2} and Cu 2p_{1/2} orbitals of Cu²⁺, respectively, while the peaks at 940.71, 943.53, and

962.05 eV corresponded to satellites [31,34]. Upon combination with AgI, the binding energies of the Cu 2p_{3/2}, Cu 2p_{1/2} characteristic peaks, and satellite peaks in 0.25-ACBV shifted to lower binding energies. Simultaneously, characteristic peaks corresponding to Cu⁺ appear at 931.53 and 951.26 eV [56]. This shift indicated that upon the formation of the AgI/Cu-BiVO₄ heterojunction, the electron cloud density around Cu increased, and a transition occurred from Cu²⁺ to Cu⁺ to maintain charge balance. Furthermore, the Cu²⁺/Cu⁺ redox pair acted as an electron trap and PMS activation site, promoting favorable charge separation dynamics and catalytic activity [57]. The Ag 3d spectra of 0.25-ACBV at 368.51 and 374.53 eV were assigned to spin-orbital fragmentation of Ag 3d_{5/2} and Ag 3d_{3/2} of Ag⁺, respectively [19] (Fig. 2d). In the I 3d spectra (Fig. 2e), the characteristic peaks of the I 3d_{5/2} and I 3d_{3/2} orbitals were located at 619.26 and 630.74 eV [17]. The positive shift of the Ag 3d and I 3d peaks in 0.25-ACBV compared to AgI indicates a decrease in electron density. This further verified the strong electronic coupling effect between AgI and Cu-BiVO₄, resulting in directional electron transfer from AgI to Cu-BiVO₄ at the heterojunction interface, thus promoting efficient carrier transfer kinetics [32]. The XPS results confirm the heterostructure effect between AgI and Cu-BiVO₄ and the appearance of oxygen vacancies.

EPR measurements confirmed the presence of oxygen vacancies within catalysts. 0.25-ACBV exhibited the strongest oxygen vacancy characteristic signal at *g* = 2.003 (Fig. 2f). The OVs structure significantly enhanced electron delocalization and transfer, promoting PMS adsorption and activation [30]. Furthermore, OVs could act as electron traps to accelerate the separation of photogenerated carriers [45]. In addition, Cu-BiVO₄ displayed a stronger EPR signal compared to BiVO₄, indicating that Cu doping induced the formation of oxygen vacancy defects that facilitated the process. The local crystal structure of the 0.25-ACBV catalyst was probed deeply by Raman spectroscopy. As displayed in Fig. S2f, the BiVO₄ spectral bands at 128 cm⁻¹ and 212 cm⁻¹, 327 cm⁻¹ and 367 cm⁻¹, and 827 cm⁻¹ were attributed to the external

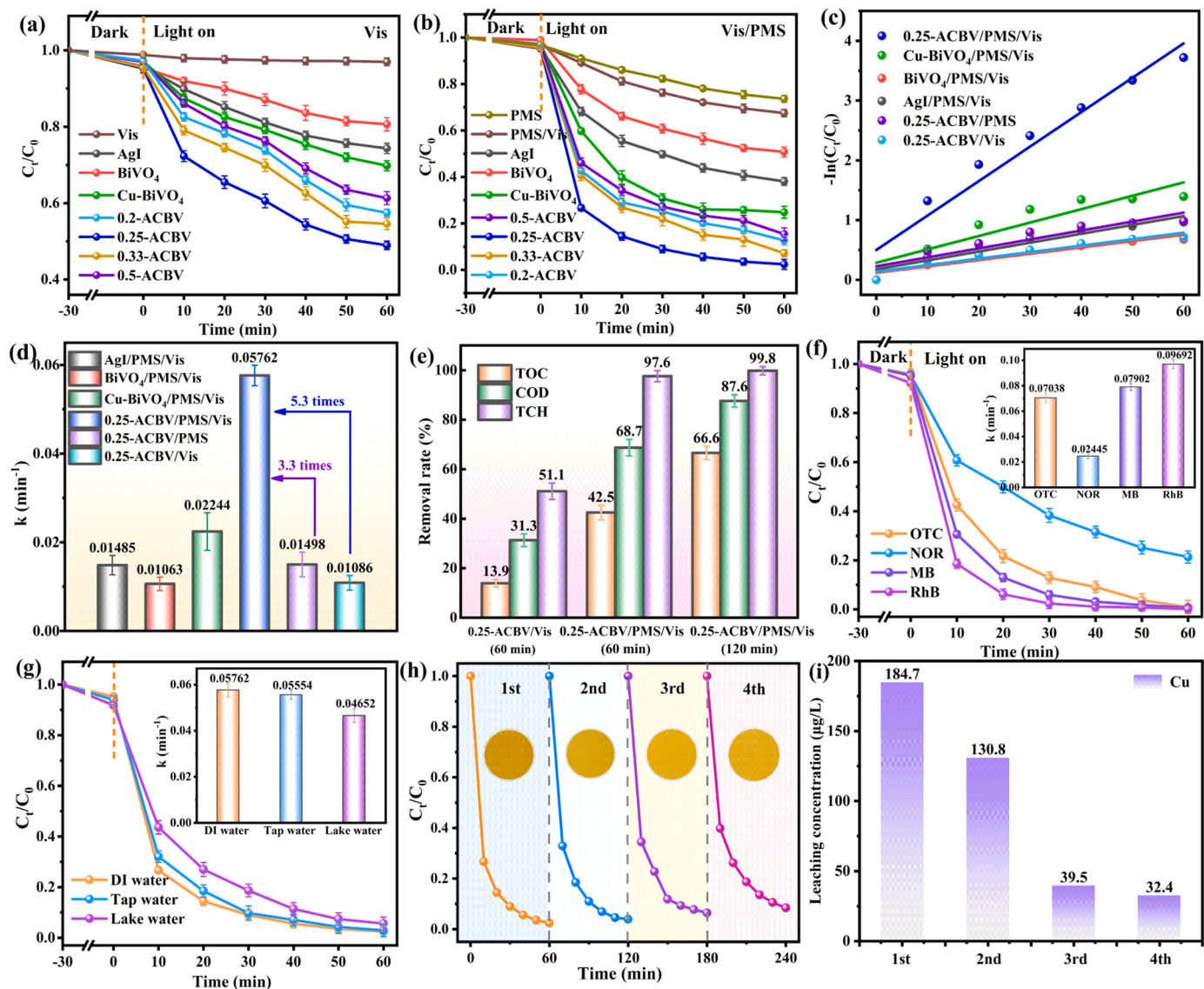


Fig. 3. The TC degradation in the (a) Vis system and (b) PMS/Vis system. (c) Pseudo-first-order kinetics and (d) rate constants in different system. (e) TOC and COD removal by 0.25-ACBV/Vis and 0.25-ACBV/PMS/Vis systems. (f) The degradation efficiency of different pollutants and (g) water bodies, the insets in Fig. 3f-g are the corresponding rate constants. (h) TC degradation and (i) leaching concentration of Cu in the 0.25-ACBV/PMS/Vis system during four cycles. (Conditions: [TC] = 20 mg/L, [Catalyst] = 0.6 g/L, [pH] = 5.6, [PMS] = 1.0 mM, [Light intensity] = 114 mW/cm²).

mode vibrations of BiVO₄, the symmetric and asymmetric stretching modes of the VO₄³⁻ tetrahedron, and the symmetric stretching mode of the V-O bond, respectively [58]. Interestingly, after copper doping, the V-O stretching band shifted to lower wavelengths (820 cm⁻¹), which was ascribed to the formation of Cu-O bonds due to the covalent binding of Cu atoms with O atoms in BiVO₄, consequently stretching the V-O bonds within the VO₄³⁻ molecule [59]. The V-O stretching band in 0.25-ACBV redshifted to 824 cm⁻¹, indicating the increase in oxygen vacancies shortens the V-O bond [60]. The shorter V-O bond length implies a larger lone-pair distortion around the Bi³⁺ cations, resulting in a greater overlap between Bi 6p and O 2p orbitals in the valence band, which contributed to the enhanced migration of photogenerated holes [61].

3.2. Photocatalytic performance evaluation

The activity of the catalyst to activate PMS-assisted visible photocatalysis was assessed by oxidative degradation of TC. Only in the visible photocatalytic system (Vis system) (Fig. 3a), the 0.25-ACBV exhibited

excellent TC photocatalytic activity (51.6%), significantly higher than that of BiVO₄ (19.4%) and AgI (25.7%), indicating that the remarkable coupling effect of the heterostructure between Cu-BiVO₄ and AgI. The Vis control experiment excluded autodegradation of TC. Interestingly, the activities of 0.33-ACBV (45.5%) and 0.5-ACBV (38.7%) were suppressed with increasing AgI loading. This may be due to the excessive aggregation of AgI hindering the active site of Cu-BiVO₄ and depressing the effective interfacial charge transfer. Remarkably, the moderate amount of Cu²⁺ doped BiVO₄ enhanced the TC photocatalytic degradation efficiency (30.2%). This confirms that the modulation of the local coordination environment of BiVO₄ by the Cu²⁺ hybridization band can reduce the energy level jumping barrier and improve the visible light absorption and mass transfer efficiency. The photocatalytic PMS activation performance of the catalysts was further investigated (Fig. 3b). The TC removal jumped to 97.6% in the 0.25-ACBV/PMS/Vis system, indicating that the optimal molar ratio of 0.25-ACBV could achieve the most optimal non-homogeneous mass transfer. Meanwhile, the removal of TC by the Cu-BiVO₄/PMS/Vis system was significantly improved since Cu²⁺/Cu⁺ acted as the main active site for PMS activation.

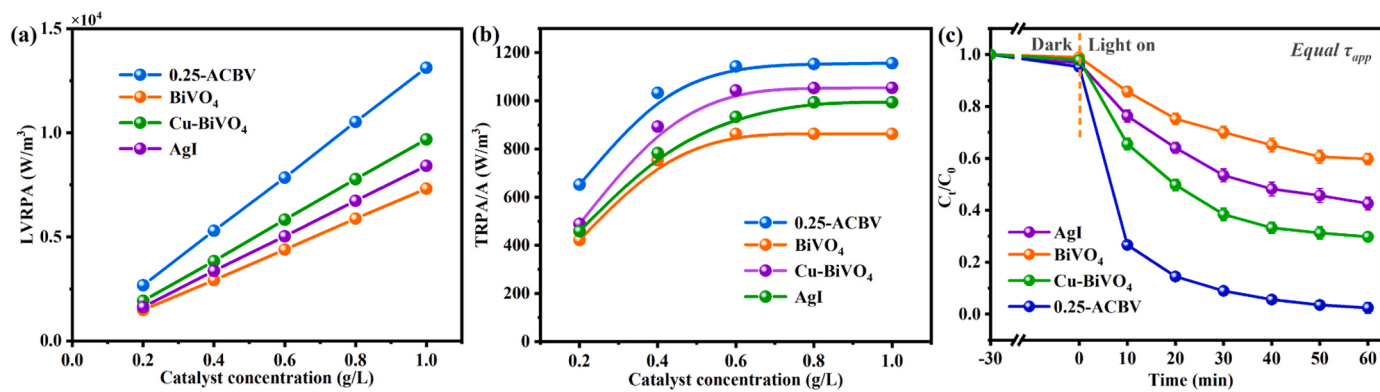


Fig. 4. (a) LVRPA on the surface at different catalyst concentrations and (b) TRPA per unit surface area under visible light irradiation as the function of possible catalyst loading. (c) photocatalytic degradation of TC by different catalyst suspensions at equal optical τ_{app} .

However, the leaching concentration of Cu ions in the Cu-BiVO₄/PMS/Vis system was notably higher than that in the 0.25-ACBV/PMS/Vis system (Fig. S3). This confirmed that the AgI component in the 0.25-ACBV composite material significantly promoted the Cu²⁺/Cu⁺ cycle and TC degradation. This was likely due to the formation of the heterojunction promoting charge transfer, which facilitated more free electrons participating in the reduction of Cu²⁺ to Cu⁺, thereby reducing the leaching of Cu ions. Interestingly, the removal of TC in the PMS system was limited (26.4%), which could be attributed to the weak oxidizing effect of PMS itself. The TC removal rate in the PMS/Vis system experienced a slight increase (32.6%), primarily due to the visible light-promoted O-O bond cleavage of PMS.

The degradation of TC by the 0.25-ACBV/PMS/Vis system was much higher than that of the 0.25-ACBV/Vis system (Fig. S4), with a reaction rate constant k (0.05762 min⁻¹) that was 3.3 times higher than that of the 0.25-ACBV/Vis system (0.01498 min⁻¹) (Fig. 3c-d). This verified that PMS contributed to the depletion of electrons and holes in the 0.25-ACBV/PMS/Vis system, which promoted the generation of ROS and shortened the overall oxidation process [12]. On the other hand, the 0.25-ACBV/PMS/Vis system showed 35% higher TC removal than the 0.25-ACBV/PMS system, and the reaction rate was 5.3 times higher than the 0.25-ACBV/PMS system (0.01086 min⁻¹). This suggests that visible light provides prerequisites for PMS activation and effective mass transfer by promoting internal charge transfer in 0.25-ACBV [32]. Overall, 0.25-ACBV compensated the charge balance, optimized the interfacial contact by exploiting the Cu²⁺/Cu⁺ redox cycle and oxygen defects, and induced the optimal synergism between visible light and PMS for the dual modulation effect of photogenerated carrier separation and PMS activation. Additionally, the coupling effect between AgI and Cu-BiVO₄ was further quantified as 3.1 using the synergy index, and the synergy effect between visible photocatalysis and PMS activation was 2.2 (See details in Text S3). This analysis confirms that the formation of AgI/Cu-BiVO₄ heterojunction has a positive synergistic effect on visible photocatalysis and PMS activation.

Table S2 lists specific degradation data from previous similar studies. Clearly, the AgI/Cu-BiVO₄ heterostructure exhibited similarly high degradation efficiencies in the PMS-assisted photocatalytic system. The mineralization of TC by 0.25-ACBV was evaluated (Fig. 3e and Table S3). Due to the accumulation and competition of numerous intermediates, the 0.25-ACBV/Vis system mineralized only 13.9% and 31.3% of TOC and COD, respectively. While, the 0.25-ACBV/PMS/Vis system achieved 66.6% and 87.6% mineralization of TOC and COD, respectively, within 120 min of reaction. Besides, the apparent quantum efficiency (AQE) of the 0.25-ACBV/PMS/Vis system for TC degradation could be further quantified as 0.51% (Text S4). The effects of catalyst dosage, pollutant concentration and PMS dosage on the degradation activity of the 0.25-ACBV/PMS/Vis system were further investigated by batch experiments (Fig. S5a-c and Text S5). Under the same

experimental condition as TC, the 0.25-ACBV/PMS/Vis system achieved impressive degradation efficiencies of 99.1%, 78.6%, 99.3% and 99.8% for OTC, NOR, MB and RhB, respectively (Fig. 3f). Obviously, these results validate the versatility of the 0.25-ACBV in the effective degradation of common pollutants through the activation of PMS. In addition, the 0.25-ACBV/PMS/Vis system exhibited broad pH adaptability (See details in Fig. S6a-b and Text S6), as well as remarkable interference resistance to co-existing ions and natural organic matter (NOM) (Fig. S6c). Tap water (Jinpan Reservoir, Heihe River) and lake water (Xingqinggong Park) were collected to further validate the potential of the system for application in real water matrices. As depicted in Fig. 3g, the removal of TC in tap and lake water media reached 97.1% and 94.3%, respectively, despite the competition of natural organic matter (such as dissolved organic matter, sulfate, residual chlorine and ions) and impurities. Remarkably, the TC degradation efficiency remained as high as 91.4% after four cycles (Fig. 3h). This result confirms the stable catalytic activation properties and photocorrosion resistance of the 0.25-ACBV heterojunction [55]. Throughout two cycles, the concentration of leached Cu ions in the 0.25-ACBV/PMS/Vis system were measured as 184.7 and 130.8 μ g/L respectively. In the following two cycles, the concentration of leached Cu ions remained stable at 39.5 and 32.4 μ g/L (Fig. 3i). This result also validated the excellent stability of the 0.25-ACBV heterojunction. To evaluate the potential contribution of leached metal ions to the catalytic reaction, related homogeneous catalysis experiments were conducted. As shown in Fig. S7, the homogeneous Cu²⁺/PMS/Vis system with different concentrations showed similar TC removal rates as the PMS/Vis system, indicating that the contribution of homogeneous catalysis to TC degradation was negligible. The XRD spectra and SEM images of 0.25-ACBV before and after the reaction showed no significant changes in the crystal structure and microscopic morphology (Fig. S8). This indicates the high stability of the 0.25-ACBV heterojunction in heterogeneous PMS activation. The above results validate the wide environmental adaptability and potential utility of the 0.25-ACBV/PMS/Vis system for practical wastewater treatment.

The study of optical properties helps to evaluate the photocatalytic activity of the catalysts more comprehensively. The optical coefficients of AgI, BiVO₄, Cu-BiVO₄ and 0.25-ACBV catalysts are shown in Table S4. The modification of AgI enhanced the light absorption properties of the 0.25-ACBV catalyst suspensions. As illustrated in Table S5 and Fig. 4a, both the optical thickness and LVRPA of the catalysts increased linearly with increasing concentration. The 0.25-ACBV sample exhibited a higher LVRPA slope, indicating its superior light absorption capability. As the catalyst concentration increases, the TRPA values displayed a gradient increase, but eventually reached a constant absorption value (Fig. 4b). Literature reports that the region of constant absorption values (TRPA variation <0.5%) is considered optimal [36]. For AgI, the optimal values were around 0.8–1.0 g/L, while BiVO₄, Cu-BiVO₄, and

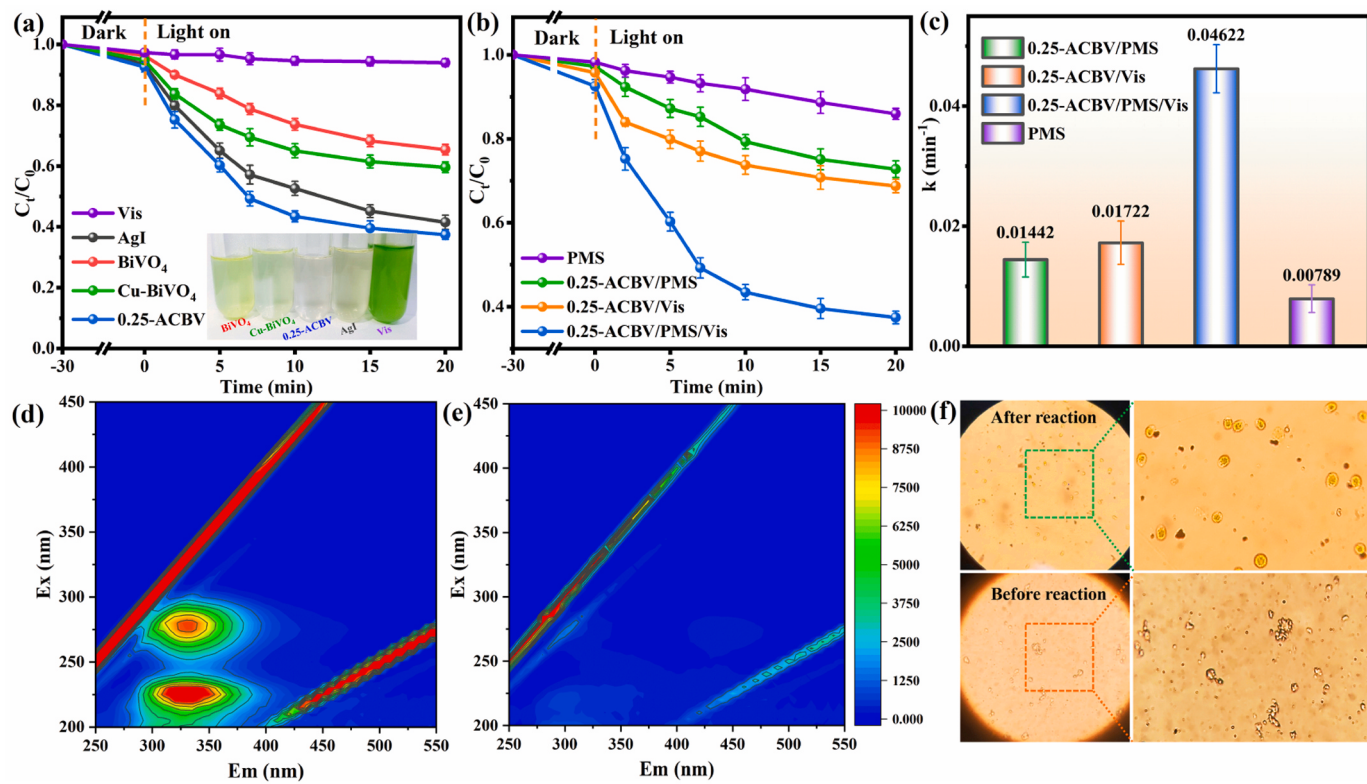


Fig. 5. PMS-activated photocatalytic performance of Chl-a removal by (a) AgI, BiVO₄, Cu-BiVO₄ and 0.25-ACBV composites, the inset is the chromatic changes of *M. aeruginosa*, (b) different systems and (c) the rate constants. (Conditions: [TC] = 20 mg/L, [Catalyst] = 0.6 g/L, [pH] = 5.6, [PMS] = 1.0 mM, [Light intensity] = 114 mW/cm²). 3D EEM fluorescence spectra of EOM of *M. aeruginosa* in the catalytic system at (d) 0 min and (e) 20 min. (f) Morphology of algal cells before and after reaction.

0.25-ACBV were approximately 0.6–0.8 g/L. Notably, the τ_{app} values corresponding to these optimal catalyst concentrations fall within the optimum optical thickness of the reactor (1.8–4.4) [36,41]. Clearly, the photon absorption of the catalyst is closely related to its τ_{app} , which directly affects pollutant degradation. To better compare the catalytic activities of different catalysts, comparative experiments were conducted at an equal τ_{app} (3.21) to the 0.25-ACBV (Fig. 4c). The experimental catalyst dosages for AgI, BiVO₄, and Cu-BiVO₄ were calculated as 0.43, 0.38, and 0.49 g/L, respectively. At equal values of τ_{app} , the 0.25-ACBV sample still exhibited the optimal TC removal ability, with a trend similar to the results that were shown in Fig. 3b, which further confirmed the effectiveness of dual modulation in the photocatalytic PMS activation system.

3.3. Photocatalytic inactivation performance of *M. aeruginosa*

Antibiotics coexisting in natural water bodies have a toxic promotion mechanism on the growth and reproduction of *M. aeruginosa*. While ROS generated during PMS activation-assisted photocatalysis induces oxidative stress and destroys algal cell structure. To further investigate the application potential of this process in controlling eutrophic water, *M. aeruginosa* inactivation tests were conducted. As depicted in Fig. 5a, within 20 min of illumination, the chlorophyll a (Chl-a) content of the visible-light-only group remained stable, suggesting no significant impact on the vital activities of *M. aeruginosa*. Under the synergistic effect at the heterojunction, 0.25-ACBV exhibited the highest photocatalytic inactivation efficiency (62.6%) on *M. aeruginosa* with PMS activation. Interestingly, the inhibitory effect of Cu-BiVO₄ on algae growth (40.3%) was superior to that of BiVO₄, confirming the toxic inhibitory effect of Cu²⁺ on algae [34]. Additionally, AgI as a photocatalyst had also exhibited a similar effect on algal inactivation as 0.25-ACBV. This is due to the inherent antibacterial and disinfection

abilities of AgI, which can bind with thiol groups in cell membranes and with DNA and RNA molecules within cells, thereby effectively inhibiting algal growth [62,63]. The color change in the inset has demonstrated that both 0.25-ACBV and AgI can effectively suppress algae growth, with 0.25-ACBV showing superior inactivation effects. Fig. 5b shows the inactivation performance of *M. aeruginosa* in different systems. Apparently, the 0.25-ACBV/PMS/Vis system removed significantly more Chl-a than the 0.25-ACBV/PMS system (27.2%) and the 0.25-ACBV/Vis system (30.3%). This verified that the 0.25-ACBV/PMS/Vis synergistic system could accelerate Cu²⁺/Cu⁺ cycling and induce dual regulation of PMS activation and effective mass transfer. This was also confirmed by the corresponding rate constants (Fig. 5c). The optimal amounts of catalyst and PMS were further determined to be 0.9 g/L and 0.75 mmol/L, respectively, for the inactivation of *M. aeruginosa* by this system (Fig. S9a-b). Under optimal conditions, the increased concentration of ROS in the 0.25-ACBV/PMS/Vis system resulted in 78.8% inhibition of algal cells, which was significantly better than other similar photocatalytic systems (Table S6).

The evolution of algal extracellular organic matter (EOM) during PMS-assisted photocatalytic inactivation was visually verified by 3D EEM analysis. As shown in Fig. 5d-e, two major fluorescence peaks located at $\lambda_{ex}/\lambda_{em} = 225/325$ nm and $\lambda_{ex}/\lambda_{em} = 275/340$ nm in the spectra corresponded to aromatic proteins and xanthates, respectively [4]. After 20 min of reaction, the intensity of the fluorescence peaks in the EEM each underwent a significant reduction, indicating that 0.25-ACBV caused serious damage to the algal cell activity. Meanwhile, the changes in peak intensity for the xanthate-like substances were smaller than those for protein-like substances, indicating that humic acid-like substances were more resistant to oxidation and degradation. In addition, Fig. 5f showed that the primitive algal cells were intact in shape, with smooth surfaces and clear boundaries. However, after 20 min of reaction, the morphology of algal cells underwent obvious

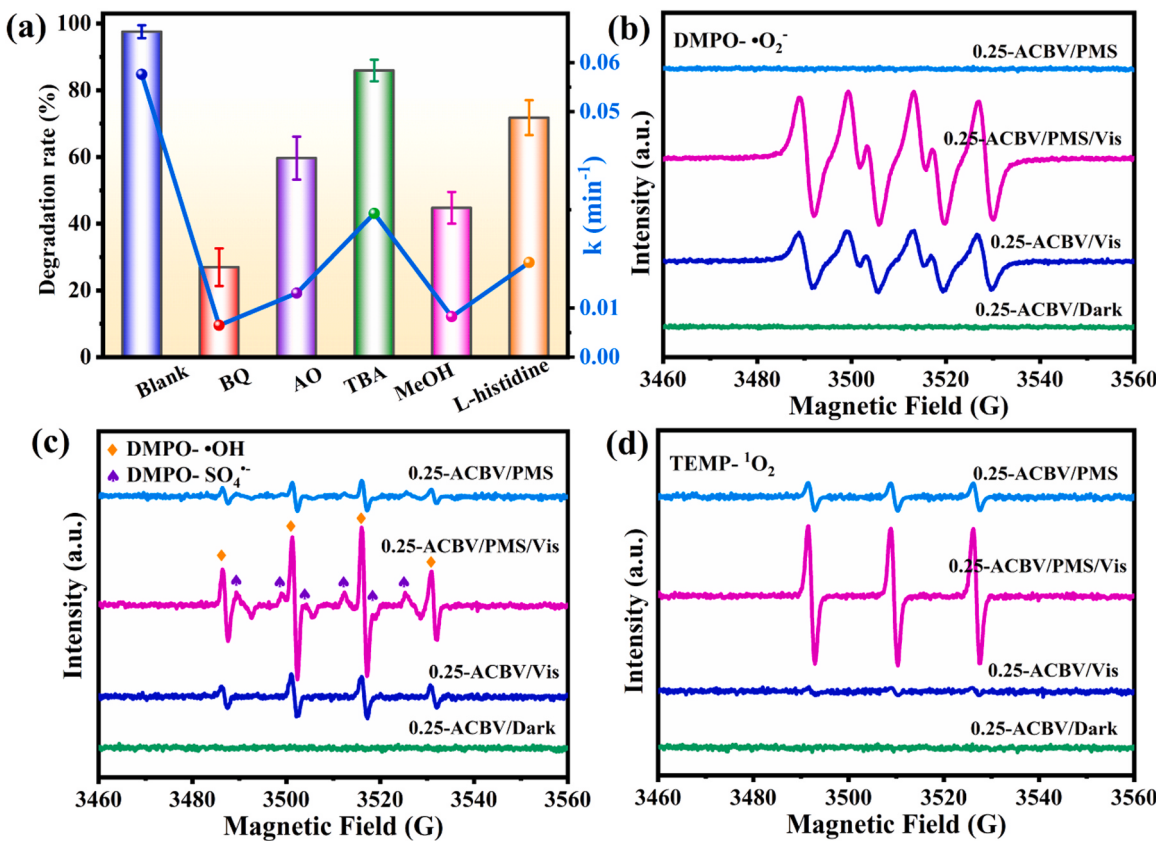


Fig. 6. (a) ROS quenching experiment of TC degradation over 0.25-ACBV in the PMS/Vis system. Conditions: [TC] = 20 mg/L, [Catalyst] = 0.6 g/L, [pH] = 5.6, [PMS] = 1.0 mM, [MeOH] = [TBA] = 500 mM, [BQ] = [L-histidine] = 1 mM, [AO] = 10 mM. EPR spectra of (b) DMPO-•O₂⁻, (c) DMPO-SO₄^{•-} and DMPO-•OH, and (d) TEMP-¹O₂.

shrinkage, cell structure was damaged, intracellular lysate exuded, and massive algal cells died. This intuitively confirmed that ROS generated by 0.25-ACBV during the PMS-activated photocatalytic process severely damaged the cell structure and effectively inactivated *M. aeruginosa*.

3.4. Possible photocatalytic mechanism

3.4.1. Identification of ROS

The ROS generated by 0.25-ACBV during the PMS activation-assisted process was elucidated by free radical scavenging experiments. MeOH was employed as a scavenger for SO₄^{•-} ($k = 1.6-7.8 \times 10^7 \text{ M}^{-1} \text{ s}^{-1}$) and •OH ($k = 1.2-2.8 \times 10^9 \text{ M}^{-1} \text{ s}^{-1}$), while TBA was used as a scavenger for •OH (k MeOH = $3.8-7.6 \times 10^8 \text{ M}^{-1} \text{ s}^{-1}$). Furthermore, BQ, AO, and L-histidine were adopted as scavengers for •O₂⁻, h⁺ and ¹O₂, respectively [12]. As shown in Fig. 6a and Fig. S10a, the addition of BQ (36.7%, $k = 0.00650 \text{ min}^{-1}$) and AO (59.6%, $k = 0.01304 \text{ min}^{-1}$) significantly inhibited the oxidation of TC, indicating the presence of •O₂⁻ and h⁺ in the system. Compared to TBA (84.9%, $k = 0.02929 \text{ min}^{-1}$), the inhibitory effect of MeOH on TC removal significantly increased (44.8%, $k = 0.00825 \text{ min}^{-1}$), highlighting the significant contribution of SO₄^{•-} to the reaction system. Moreover, the degradation efficiency of TC was reduced by the addition of L-histidine (71.5%, $k = 0.01928 \text{ min}^{-1}$), suggesting the possible involvement of non-radical ¹O₂ in the oxidative degradation of the pollutant. However, the reaction between L-histidine and PMS could not be neglected [64]. Fig. S10b displayed the effects of different amounts of L-histidine on TC degradation, revealing relatively minor influences and implying that the primary inhibitory role of L-histidine was the capture of ¹O₂. Similarly, FFA ($k = 1.2 \times 10^8 \text{ M}^{-1} \text{ s}^{-1}$) and β-carotene ($k = 2-3 \times 10^{10} \text{ M}^{-1} \text{ s}^{-1}$) were employed as ¹O₂ scavengers, further confirming the presence of ¹O₂ [65,66]. Apparently, the inhibitory effect of FFA and β-carotene on TC degradation

demonstrated the involvement of ¹O₂ in the degradation process of TC (Fig. S10c). As depicted in Fig. S10d, under an N₂ atmosphere, the 0.25-ACBV/PMS/Vis system maintained a certain level of degradation activity, indicating that ¹O₂ mainly originated from the 0.25-ACBV activation of PMS rather than dissolved oxygen in water [67,68]. The above results suggest that the 0.25-ACBV/PMS/Vis system can promote the generation of •O₂⁻, h⁺, SO₄^{•-} and ¹O₂.

Subsequently, the ROS generation and quantitative information were further verified by EPR testing. In Fig. 6b, the DMPO-•O₂⁻ signal of the 0.25-ACBV/Vis system, indicating that the energy band modulation of BiVO₄ by AgI and Cu²⁺ optimized the interfacial contacts and facilitated efficient charge transfer [55]. And the enhanced DMPO-•O₂⁻ signal in the 0.25-ACBV/PMS/Vis system verified the synergistic effect between photocatalysis and PMS activation. Only the DMPO-•OH signal was detected in the 0.25-ACBV/Vis system, whereas the 0.25-ACBV/PMS/Vis system revealed the dual peaks of DMPO-SO₄^{•-} and DMPO-•OH (Fig. 6c). This confirms that 0.25-ACBV in visible light synergistically promotes PMS activation to generate SO₄^{•-}/•OH. Notably, the weak signals of the 0.25-ACBV/PMS system illustrated the activation of PMS by 0.25-ACBV. Similarly, the higher signal of TEMP-¹O₂ in the 0.25-ACBV/PMS/Vis system over the 0.25-ACBV/PMS system (Fig. 6d), confirming the promotion of PMS self-decomposition by visible light [12]. No obvious ¹O₂ signal was detected in the 0.25-ACBV/Vis system, implying that PMS dominated the generation of non-radical ¹O₂ [13]. Apparently, the 0.25-ACBV heterojunction could generate abundant reactive oxygen species under the synergistic effect of photocatalysis and PMS activation, resulting in high-efficiency degradation performance.

Competitive kinetic experiments of NB (a chemical probe for •OH, ($k_{\text{•OH+NB}} = 3.9 \times 10^9 \text{ M}^{-1} \text{ s}^{-1}$)), BA (probe for •OH ($k_{\text{•OH+BA}} = 5.9 \times 10^9 \text{ M}^{-1} \text{ s}^{-1}$) and SO₄^{•-} ($k_{\text{SO}_4^{\bullet-}+\text{BA}} = 1.2 \times 10^9 \text{ M}^{-1} \text{ s}^{-1}$), FFA (a probe both

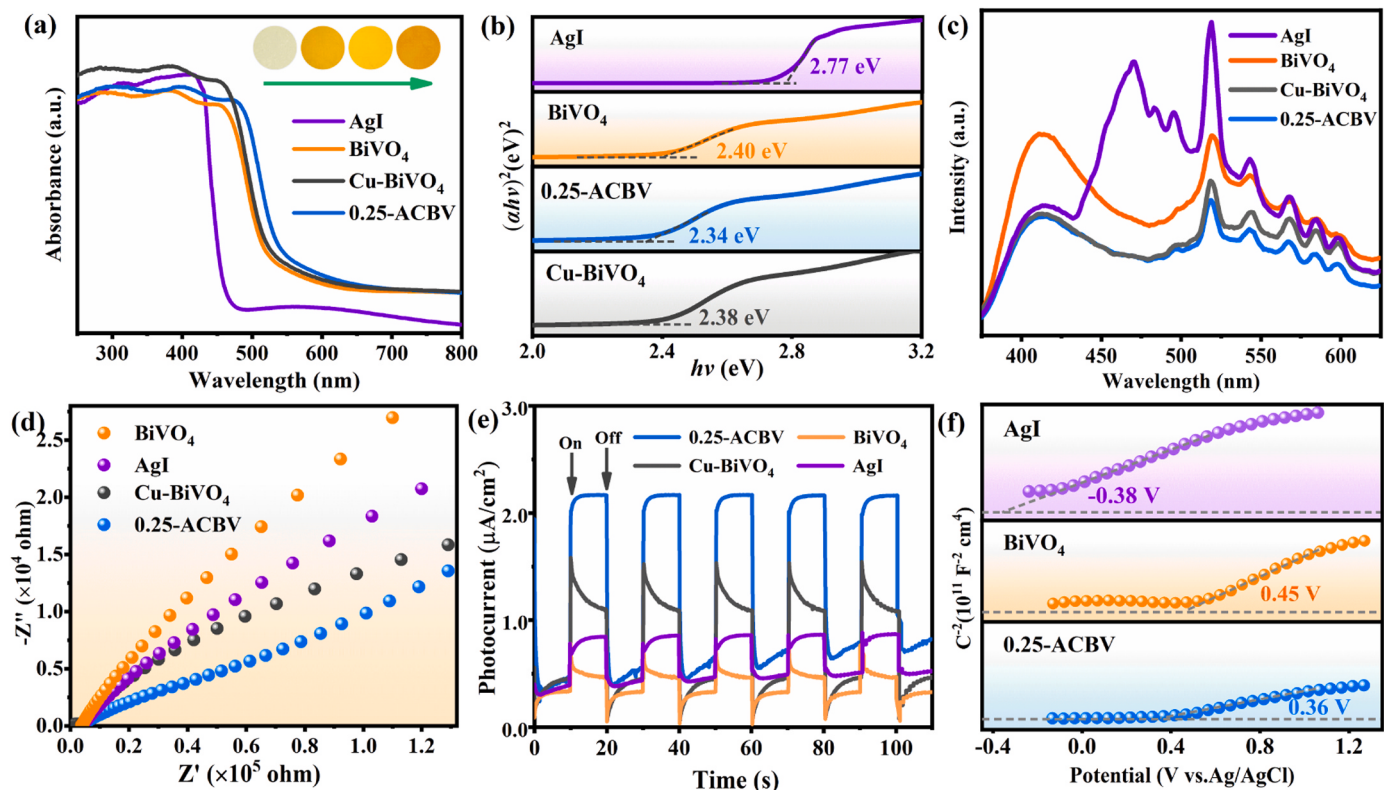


Fig. 7. (a) UV-vis DRS, (b) E_g values, (c) PL spectra with the excitation wavelength of 425 nm, (d) EIS Nyquist plots and (e) transient photocurrent responses of AgI, BiVO₄, Cu-BiVO₄ and 0.25-ACBV. (f) Mott-Schottky plots of AgI, BiVO₄ and 0.25-ACBV.

•OH ($k_{\bullet\text{OH}+\text{FFA}} = 3.6 \times 10^9 \text{ M}^{-1} \text{ s}^{-1}$) and ${}^1\text{O}_2$ ($k_{\bullet\text{O}_2+\text{FFA}} = 1.2 \times 10^8 \text{ M}^{-1} \text{ s}^{-1}$)), and TC further quantified the relative contribution of ROS to TC degradation in the 0.25-ACBV/PMS/Vis system [68,69]. As depicted in Fig. S11 and Text S1, the degradation of NB, BA, and FFA followed pseudo-first-order kinetic models, with rate constants of 0.00273 min^{-1} , 0.01204 min^{-1} , and 0.00813 min^{-1} , respectively. Consequently, the steady-state concentrations of •OH, SO_4^{2-} , and ${}^1\text{O}_2$ in the 0.25-ACBV/PMS/Vis system were calculated to be $1.17 \times 10^{-14} \text{ M}$, $1.10 \times 10^{-12} \text{ M}$, and $7.79 \times 10^{-13} \text{ M}$, respectively. The second-order rate constants for the reactions of TC with •OH and SO_4^{2-} were determined to be $4.6 \times 10^9 \text{ M}^{-1} \text{ s}^{-1}$ ($k_{\bullet\text{OH}+\text{TC}}$) and $2.2 \times 10^9 \text{ M}^{-1} \text{ s}^{-1}$ ($k_{\text{SO}_4^{2-}+\text{TC}}$), respectively [70]. Thus, the estimated relative contributions of •OH, SO_4^{2-} , and other ROS (mainly $\bullet\text{O}_2$, h^+ and ${}^1\text{O}_2$) to TC degradation were 5.6%, 25.2%, and 69.2%, reinforcing that $\bullet\text{O}_2$, h^+ , SO_4^{2-} and ${}^1\text{O}_2$ collectively dictated the oxidative process of the pollutant.

3.4.2. Optoelectronic properties

The performance of PMS-enhanced photocatalytic correlates closely with the optical properties, and charge migration behavior of the catalyst. Therefore, the optical absorption properties were investigated (Fig. 7a). Strong visible light absorption was displayed at 463 nm for AgI and 540 nm for BiVO₄ [18,20]. Compared to BiVO₄, Cu-BiVO₄ exhibited a redshift in the light absorption edge (550 nm), increased absorption intensity, and a visible color change from deep yellow to bright yellow. This was mainly ascribed to charge transfers between Cu²⁺ and the conduction or valence bands of BiVO₄ [29]. On the other hand, Cu²⁺ doping induced the formation of OVs, which acted as defect energy levels, promoting enhanced light absorption and charge separation in Cu-BiVO₄ [27,31]. As for 0.25-ACBV, its visible light response region was further effectively broadened (554 nm) due to the coupling effect between AgI and Cu-BiVO₄. Based on the Kubelka-Munk function, the bandgaps (E_g) of AgI, BiVO₄, Cu-BiVO₄ and 0.25-ACBV (Fig. 7b) were determined to be 2.77 eV, 2.40 eV, 2.38 eV, and 2.34 eV, respectively

[71,72]. Obviously, the visible light absorption response and catalytic effect of the 0.25-ACBV heterojunction are effectively enhanced by the doping of Cu²⁺ and the introduction of AgI.

The carrier separation and transfer properties of the catalytic process were further investigated. As depicted in Fig. 7c, compared to the pristine BiVO₄, the PL spectrum intensity of Cu-BiVO₄ was significantly reduced, affirming that the presence of Cu²⁺ doping states and OVs could capture photogenerated electrons in the BiVO₄ conduction band, facilitating charge carrier separation and transfer while effectively suppressing carrier recombination [31,34]. The lowest PL emission peak in 0.25-ACBV indicated the highest efficiency for photogenerated carrier separation [45]. Combined with the morphology and XPS analyses of 0.25-ACBV, it was confirmed that the constructed heterojunction structure promoted electron transfer from AgI to Cu-BiVO₄, accelerating carrier transfer. Notably, the smaller EIS arc radius of 0.25-ACBV (Fig. 7d) also substantiated the highest charge transfer rate at the 0.25-ACBV heterojunction interface [52]. Additionally, as shown in Fig. 7e, 0.25-ACBV exhibited the highest photocurrent response intensity, which was 7.2 times, 3.4 times, and 2.3 times greater than that of BiVO₄, Cu-BiVO₄, and AgI, respectively. This result indicated that the 0.25-ACBV heterojunction possessed enhanced photogenerated carrier separation properties [32]. These findings further validated the construction of the heterostructure between AgI and Cu-BiVO₄, which contributed to improved separation and migration capabilities of interfacial photogenerated charges, thus accelerating the catalytic reaction process.

3.4.3. Electron transfer mechanism of S-scheme heterojunction

The band structure of the sample was investigated by Mott-Schottky (M-S) curves. Typically, the carrier densities are negatively correlated with the slope of the M-S curve [71]. As depicted in Fig. 7f, the lower slope of the curve for 0.25-ACBV implies that Cu²⁺ doping and AgI coupling notably enhanced the carrier density of 0.25-ACBV.

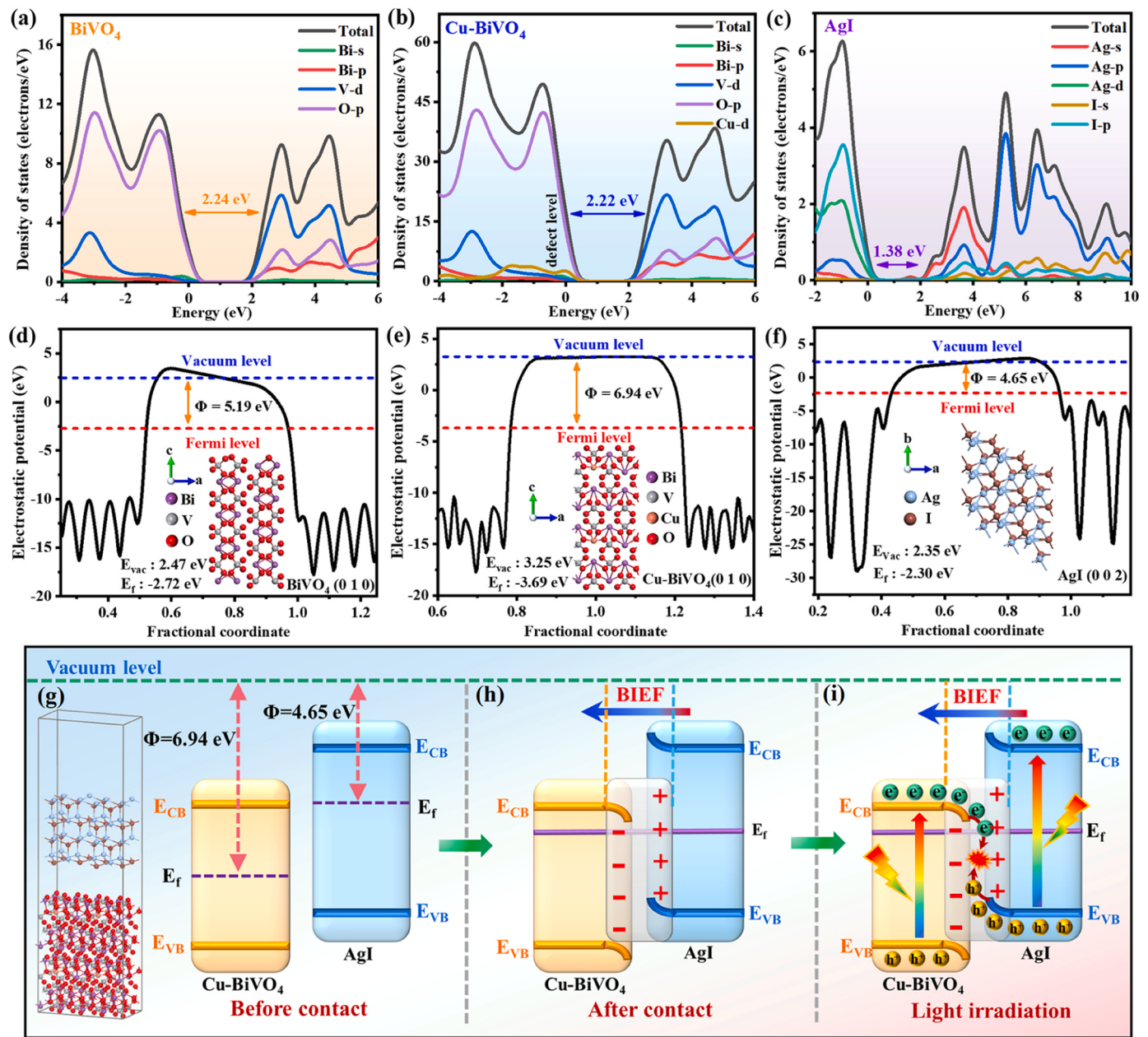


Fig. 8. The partial density of states (PDOS) for (a) BiVO₄, (b) Cu-BiVO₄ and (c) AgI. The electrostatic potentials of (d) BiVO₄ (010), (e) Cu-BiVO₄ (010) and (f) AgI (002). schematic illustration of the S-scheme photogenerated charge-transfer pathway of AgI/Cu-BiVO₄: (g) before contact, (h) after contact in darkness and (i) contact under light irradiation.

Meanwhile, the positive slopes of the curves confirm the n-type semiconductor properties of BiVO₄ and AgI [73]. The conduction band potentials (E_{CB}) of BiVO₄ and AgI were 0.35 eV and -0.48 eV (vs. NHE), respectively, and the corresponding valence band potentials (E_{VB}) of 2.75 eV and 2.29 eV (vs. NHE) were obtained. (See details in Text S7 and Table S7). Fig. S12 illustrates that the AgI and BiVO₄ semiconductors have matched and staggered energy band arrangements. The accumulated photogenerated electrons in the CB of BiVO₄ (+0.35 eV vs. NHE) are insufficient to convert O₂ to •O₂⁻ radicals (-0.33 eV vs. NHE) (Fig. S13) [9]. This inconsistency with the results of quenching experiments and EPR. Thus, the conventional Type-II heterojunction pathway cannot adequately explain the charge transfer. By contrast, AgI as an RP photocatalyst with CB (-0.48 eV vs. NHE) is sufficient to produce •O₂⁻. Therefore, the internal charge transfer mode in the AgI/Cu-BiVO₄ heterojunction is more inclined to follow the S-scheme heterojunction mechanism, formed by BiVO₄ as the OP and AgI as the RP photocatalyst

[27,73,74].

The formation mechanism of S-scheme AgI/Cu-BiVO₄ heterojunction and the intrinsic kinetics of interfacial charge transfer were elucidated by using DFT calculations and In-situ XPS. Fig. S14 displays the optimized geometries of BiVO₄, Cu-BiVO₄ and AgI, confirming the carrier transfer in VO₄ and the substitutional doping of Cu on the Bi site (See details in Text S8). Cu-BiVO₄ (2.22 eV) showed a lower theoretical band gap (2.24 eV) than BiVO₄ (Fig. S15-S17), indicating that the Cu doping energy level optimizes the electronic structure and exerts a broadening effect on the visible spectral response [31]. Additionally, the calculation of the band structures confirms the direct transition semiconductor properties of BiVO₄, Cu-BiVO₄, and AgI. The partial density of states (PDOS) of BiVO₄, Cu-BiVO₄ and AgI are shown in Fig. 8a-c. The primary process of BiVO₄ light absorption is the excitation of electrons from the O 2p states to the V 3d states. Notably, Cu-BiVO₄ appears as an in-gap energy state above the valence band of Cu 3d and O 2p impurity

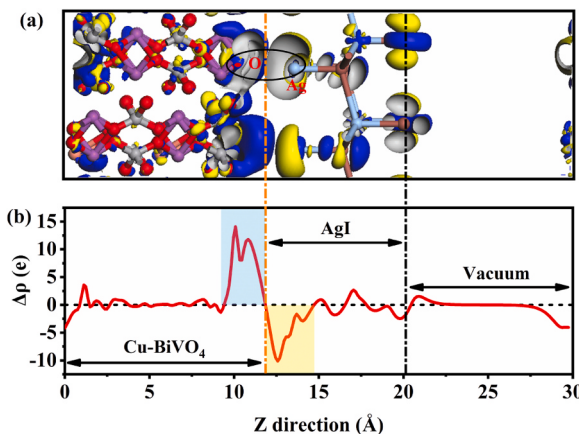


Fig. 9. (a) Charge density difference of AgI (002)/Cu-BiVO₄ (010) heterojunction, the yellow and blue areas represent charge depletion and accumulation, respectively. (b) The calculated $\Delta\rho$ across the x-y plane layers for the AgI (002)/Cu-BiVO₄ (010).

states. This confirmed that Cu²⁺ doping creates defect energy levels that can act as electron traps, lowering the energy level jump potential barrier and thus enhancing charge separation and transport [31]. The CBM and VBM of AgI are mainly composed of Ag 5 s and 1 5p states, respectively [72], which implies that carriers inside the heterojunction can be transferred from the V 3d orbitals of Cu-BiVO₄ to the I 5p orbitals of AgI. The DFT simulation reveals the internal electronic structure and carrier migration pathways of BiVO₄, Cu-BiVO₄ and AgI at the orbital level.

Furthermore, surface work function calculations contribute to interpreting the interfacial charge directional transfer. As depicted in Fig. 8d-f, the work functions (ϕ) of BiVO₄ (010), Cu-BiVO₄ (010) and AgI (002) are determined to be 5.199 eV, 6.946 eV, and 4.652 eV, respectively. The difference in the work function drives the charge

migration at the AgI/Cu-BiVO₄ interface [74]. Clearly, the Fermi energy level (E_F) of AgI (-2.30 eV) is higher than that of Cu-BiVO₄ (-3.69 eV). When Cu-BiVO₄ and AgI form an intimate heterojunction in the dark (Fig. 8g), the charges are spontaneously rearranged driven by the energy band difference, with charge transfer occurring from AgI to Cu-BiVO₄ until E_F equilibrium is established [9]. Under electrostatic interactions, the energy band of AgI bends upward due to electron loss, while the interface region of Cu-BiVO₄ bends downward due to electron accumulation. Eventually, a built-in electric field (BIEF) in the direction from AgI to Cu-BiVO₄ is formed at the AgI/Cu-BiVO₄ interface (Fig. 8h) [71]. XPS results also confirmed that this charge transfer pathway led to a decrease in the electron density on the AgI side and an enhancement on the Cu-BiVO₄ side. Both Cu-BiVO₄ and AgI are excited by visible light, and under the driving force of BIEF and band bending, photogenerated electrons on the CB of Cu-BiVO₄ recombine with holes in the VB of AgI (Fig. 8i). The directed migration through the S-scheme transfer pathway effectively promotes the separation kinetics of the interface photo-generated carriers, thereby endows the PMS-activated photocatalytic reaction with enhanced redox capability.

Fig. 9a shows the three-dimensional charge differential density difference at the AgI (002)/Cu-BiVO₄ (010) interface. Apparently, strong interactions occurred at the interface, forming an Ag-O bond electron transfer bridge, which facilitated the spontaneous electron transport from the AgI (002) surface to the Cu-BiVO₄ (010) surface [75]. This coupling effect at the heterojunction interface effectively promoted charge separation and transfer. To further characterize the electron displacement, the plane $\Delta\rho$ along the Z-axis direction is shown in Fig. 9b. The electrons flowed from the AgI (002) plane towards the Cu-BiVO₄ (010) plane [76]. This results in an upward bending for AgI (002) energy band and a downward bending for Cu-BiVO₄ (010) energy band, establishing a directional BIEF from AgI to Cu-BiVO₄.

The interfacial behavior of the heterojunction and the charge compensation effect of Cu²⁺/Cu⁺ were verified by In-situ XPS. As shown in Fig. 10a-b, the spectra of Bi 4f and V 2p of the 0.25-ACBV heterojunction shifted towards higher binding energies after visible light

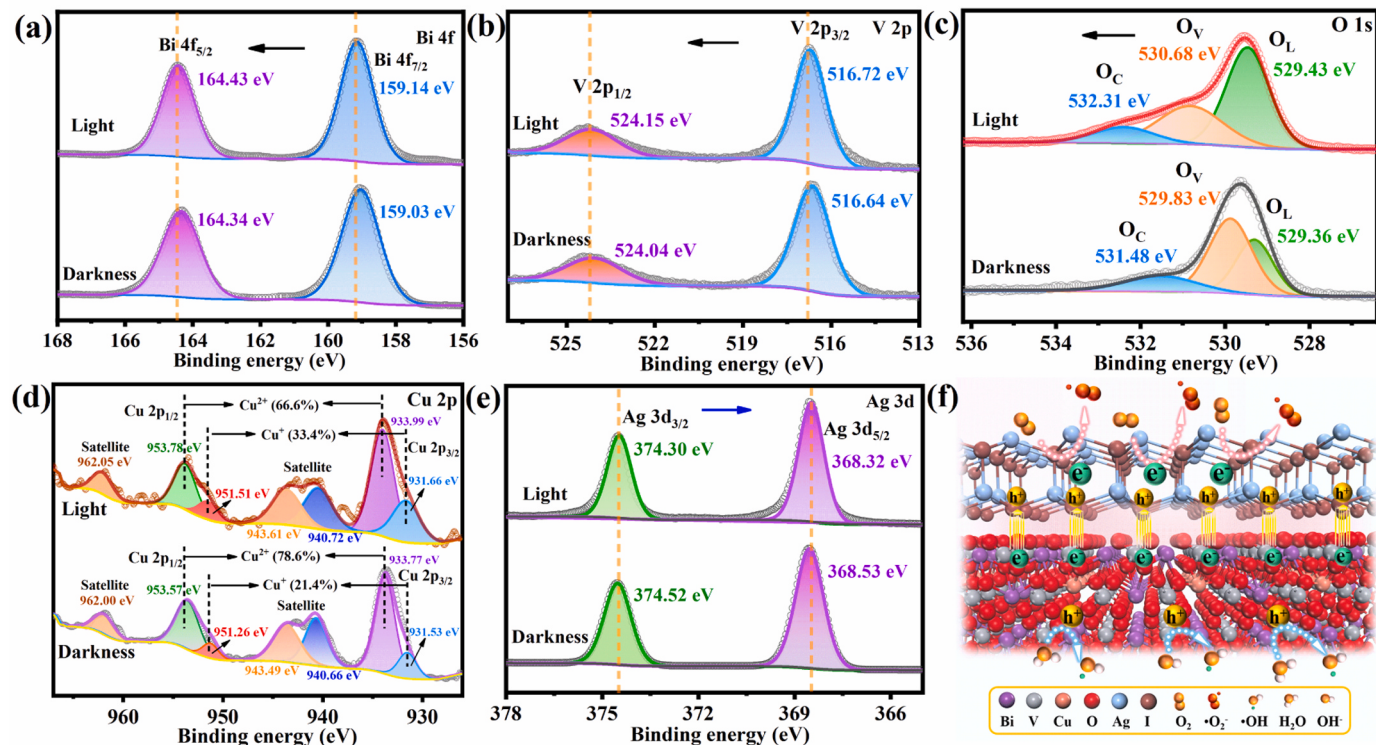


Fig. 10. In-situ XPS spectra for (a) Bi 4f, (b) V 2p, (c) O 1s, (d) Cu 2p and (e) Ag 3d of 0.25-ACBV in darkness and under visible light irradiation. (f) Schematic illustration of interfacial electron transfer between Cu-BiVO₄ and AgI under visible light irradiation.

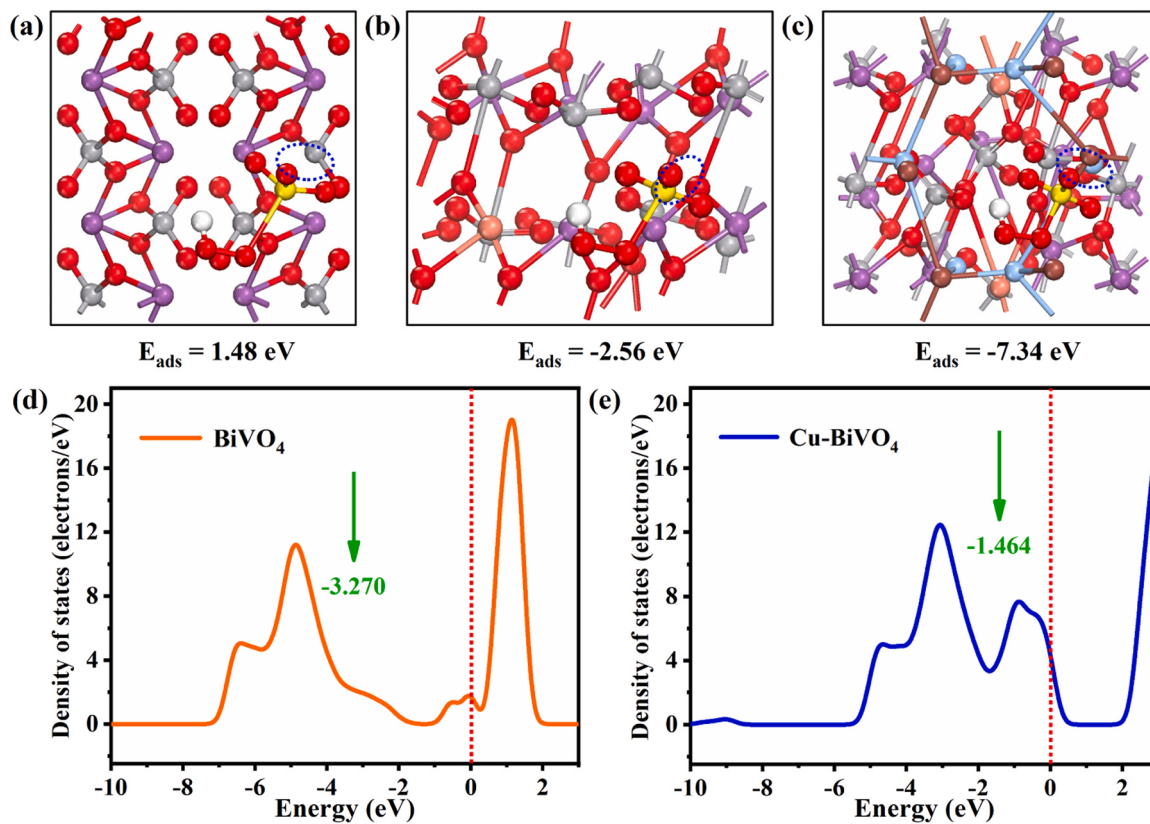


Fig. 11. Optimized geometries of PMS adsorption on the surfaces of (a) BiVO₄, (b) Cu-BiVO₄ and (c) AgI/Cu-BiVO₄ (top view). Purple, gray, yellow, red, blue, brown and white spheres represent Bi, V, Cu, O, Ag, I and H atoms, respectively. The DOS and D-band centers of (d) BiVO₄ and (e) Cu-BiVO₄.

irradiation, while the Ag 3d and I 3d spectra shifted towards lower binding energies by about 0.2 eV (Fig. 10e and Fig. S18). This result indicates that under irradiation, BIEF, energy band bending and Coulomb interactions accelerate the complexation of electrons in the CB of Cu-BiVO₄ with holes in the VB of AgI, and the S-scheme charge transfer mechanism promotes the electron depletion of Cu-BiVO₄ and the aggregation of AgI [77]. Moreover, the binding energies of the O_L and O_V fitted peaks in the O 1 s spectra of 0.25-ACBV were significantly

shifted to higher binding energies, indicating that photoinduced electrons are transferred from Cu-BiVO₄ to AgI through defective oxygen and lattice oxygen channels [73,77] (Fig. 10c). Notably, the relative content of O_V dropped sharply from 50.5% to 34.2% upon irradiation (Table S8 and Fig. S19). This further demonstrated that surface OVs could capture photogenerated electrons as PMS activation sites and directly participate in the photocatalytic and PMS activation processes, resulting in the loss of OVs [30,45]. Similarly, a positive shift was

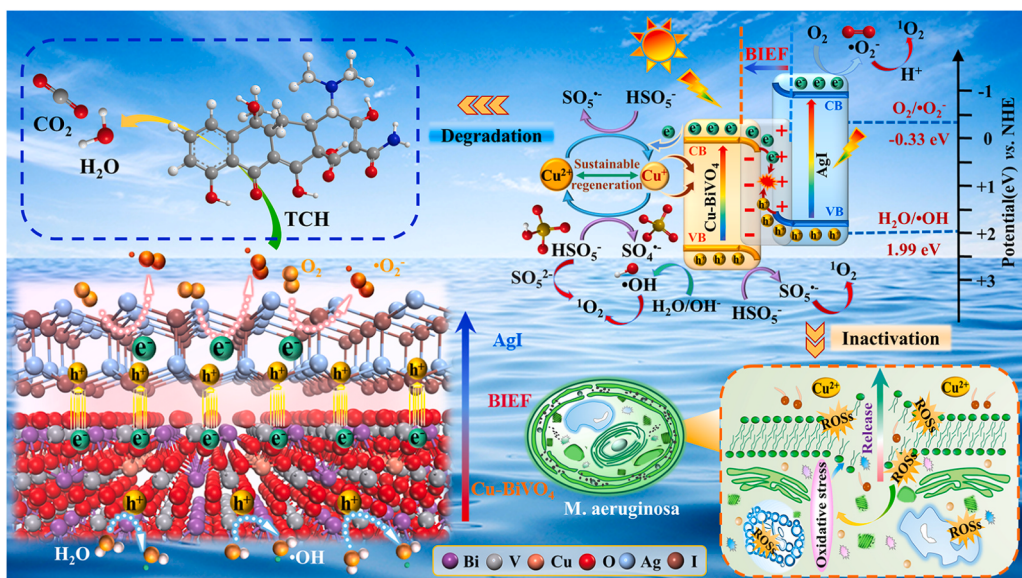


Fig. 12. Possible reaction mechanism for TC degradation and *M. aeruginosa* inactivation in AgI/Cu-BiVO₄/PMS/Vis system.

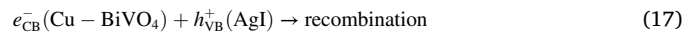
observed in the binding energy positions of the Cu 2p spectra after irradiation (Fig. 10d). By integrating the method in Table S9 [32], the proportion of Cu²⁺ species decreased from 78.6% to 66.6%, while that of Cu⁺ species increased from 21.4% to 33.4%. Apparently, the formation of the heterojunction greatly accelerated the partial conversion of Cu²⁺ to Cu⁺ under visible light. The charge balance was compensated by Cu²⁺/Cu⁺ cycling and oxygen defects, which enhanced the effective mass transfer of the PMS activation process. Fig. 10f illustrates the interface interaction and photoinduced charge migration pathway between Cu-BiVO₄ and AgI driven by BIEF. The DFT simulation and In-situ XPS results jointly verified that the S-scheme heterojunction charge transfer process and the redox cycling of Cu²⁺/Cu⁺ pairs, ensure that the AgI/Cu-BiVO₄ photocatalyst possesses excellent redox ability and carrier separation kinetics. This provides a strong driving force for the progression of PMS activation photocatalytic reactions.

Oxygen vacancy structures can facilitate the strong coupling of catalysts with surface-adsorbed oxygen [78]. To probe the promotion mechanism of OVs in the catalyst for ROS generation, O₂-TPD was utilized to measure the oxygen adsorption capacity of the samples, with the results displayed in Fig. S20. Notably, as compared to Cu-BiVO₄, 0.25-ACBV exhibited a stronger desorption peak in the low-temperature region (<400°C), which corresponded to the release of surface oxygen molecules or surface active oxygen species. This result confirmed that the increase in OVs within 0.25-ACBV contributed to the enhanced oxygen adsorption capacity and the production of •O₂⁻, thereby promoting the catalytic oxidation of pollutants [79]. To reveal the catalytic mechanism of PMS activation by OVs on the catalyst surface under visible light, the adsorption models of PMS on the oxygen-defect sites of BiVO₄, Cu-BiVO₄, and AgI/Cu-BiVO₄ were investigated. Apparently, the OVs sites in the Cu-BiVO₄ model showed higher adsorption energies (E_{ads}) (-2.56 eV) compared with those of BiVO₄ (-1.48 eV) (Fig. 11a-b). This indicated that Cu doping induced the formation of more OVs, which significantly promoted the adsorption of PMS on the catalyst surface [15]. Simultaneously, as depicted in Fig. 11d-e, the D-band center of Cu-BiVO₄ (-1.646 eV) was closer to the Fermi level than that of BiVO₄ (-3.270 eV), thus facilitating the catalytic process [80]. Moreover, PMS on AgI/Cu-BiVO₄ exhibited the highest E_{ads} (-7.34 eV) (Fig. 11c). This confirmed that the heterojunction interface promoted the adsorption activation of the O-O bond in PMS on the AgI/Cu-BiVO₄ surface through electron transfer [45].

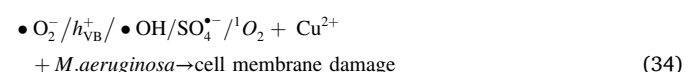
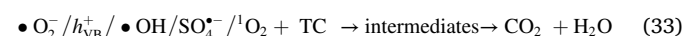
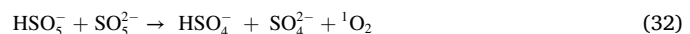
3.4.4. Possible reaction mechanism in AgI/Cu-BiVO₄/PMS/Vis system

Based on the above theoretical and experimental analyses, rational charge transfer pathways and activation mechanisms for mineralizing TC and inactivating *M. aeruginosa* in the AgI/Cu-BiVO₄/PMS/Vis system were proposed. As displayed in Fig. 12, the electrons in the VB of Cu-BiVO₄ and AgI are visibly excited and subsequently migrate into the CB (Eq. (16)). Driven by the BIEF, energy band bending, and Coulomb force, photoinduced electrons in the CB of Cu-BiVO₄ at the heterojunction interface readily recombine with photoinduced holes in the VB of AgI (Eq. (17)). Under the internal charge transfer pathways of the S-scheme, highly reducing electrons accumulating in the CB of AgI efficiently capture adsorbed O₂, generating the •O₂⁻ (Eq. (18)). Simultaneously, strongly oxidizing holes enriched in the VB of Cu-BiVO₄ can generate •OH radicals with H₂O/OH⁻ or directly oxidize pollutants (Eqs. (19 and 20)). Moreover, doped Cu²⁺ acts as an electron trap center to trap photoinduced electrons, generating Cu⁺ species. Cu⁺ further transfers to adsorbed O₂ molecules and participates in the •O₂⁻ generation (Eqs. (21 and 22)). Additionally, surface OVs can enhance the surface oxygen adsorption capacity of the catalyst. Meanwhile, OVs capture photo-generated electrons to react with adsorbed oxygen to generate •O₂⁻ and further ¹O₂ in the presence of •OH (Eq. (23) [45]). The Cu²⁺/Cu⁺ redox conversion and surface oxygen defects compensated the charge balance and significantly accelerated the interfacial charge separation. Evidently, the unique S-scheme electron transfer pathway significantly improves the interfacial charge separation and transfer kinetic, ensuring

the high redox capacity of the system, which greatly facilitates the catalytic reaction process.



The addition of PMS contributes to maximizing the consumption of additional electrons from the system to generate SO₄^{•-} and •OH (Eqs. (24 and 25)) [13,81]. In turn, holes act as electron donors to react with PMS to produce weakly oxidatively active SO₅^{•-} (Eq. (26)), and further converted into highly reactive ¹O₂ non-radicals (Eq. (27)) [82]. This process promotes the dual regulation of charge separation and PMS activation. Meanwhile, Cu²⁺, as the key active site, accelerates the induction of PMS activation, enhances SO₄^{•-} and SO₅^{•-} yields, and promotes Cu²⁺/Cu⁺ interconversion (Eqs. (28 and 29) [32]). Furthermore, the surface OVs acted as active sites to promote the adsorption activation of PMS on the AgI/Cu-BiVO₄ surface and induced the generation of SO₄^{•-} and effective mass transfer via interfacial electron transfer (Eqs. (30 and 31)) [12,30]. The ¹O₂ non-radicals can be generated by the PMS self-decay (pH > 9.3) (Eq. (32)) [81]. In summary, the free radicals and non-radical species generated during the PMS-activated photocatalytic process collectively accelerate the oxidative degradation of TC into smaller organic intermediates, ultimately inducing mineralization to CO₂ and H₂O (Eq. (33)). Similarly, these ROS groups disrupt algal cell membrane structures via oxidative stress, accelerating cell damage and leakage of intracellular organic matter [4]. In addition, the ion toxicity of low-concentration Cu²⁺ synergistically inhibits algal cell development, ultimately leading to the death of *M. aeruginosa* (Eq. (34)) [34].



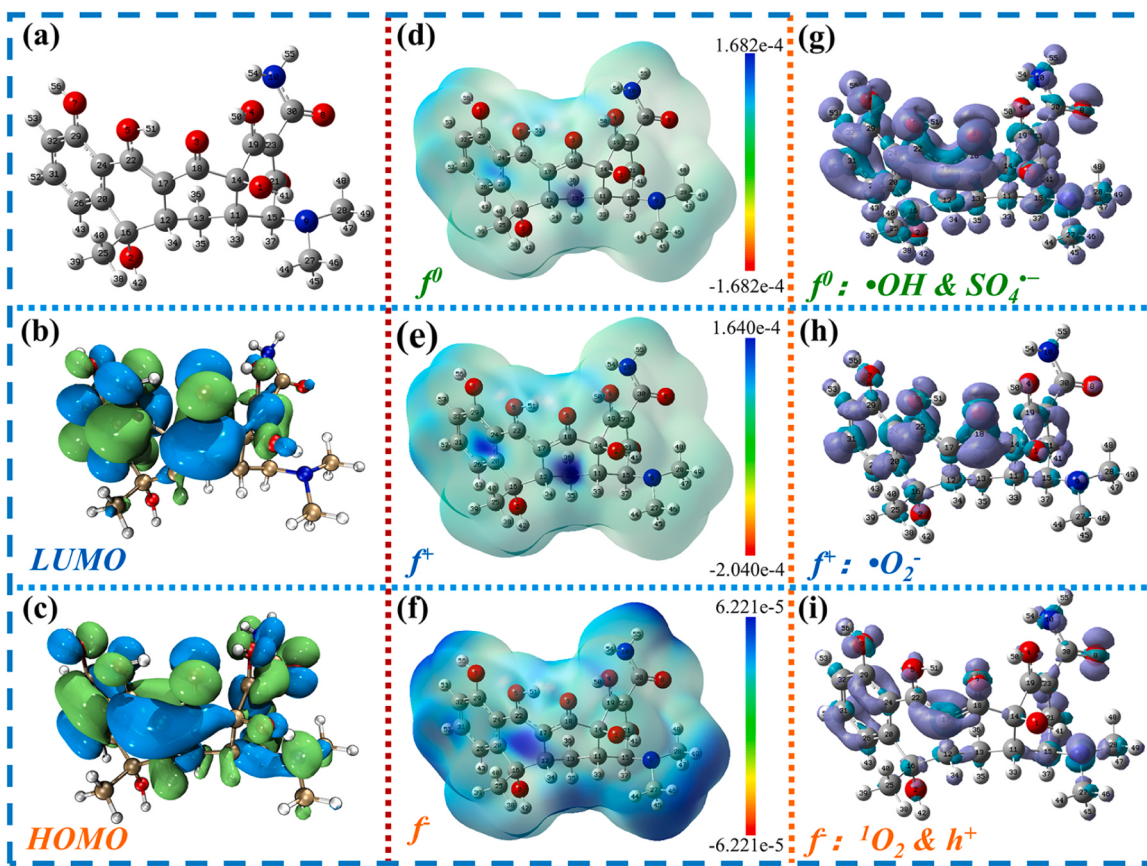


Fig. 13. (a) Optimized structure of TC. (b) HOMO and (c) LUMO for TC molecule. ESP diagram of the TC Fukui index mapping of (d) f^0 , (e) f^+ and (f) f^- . The electron density isosurface mapping of (g) f^0 , (h) f^+ and (i) f^- .

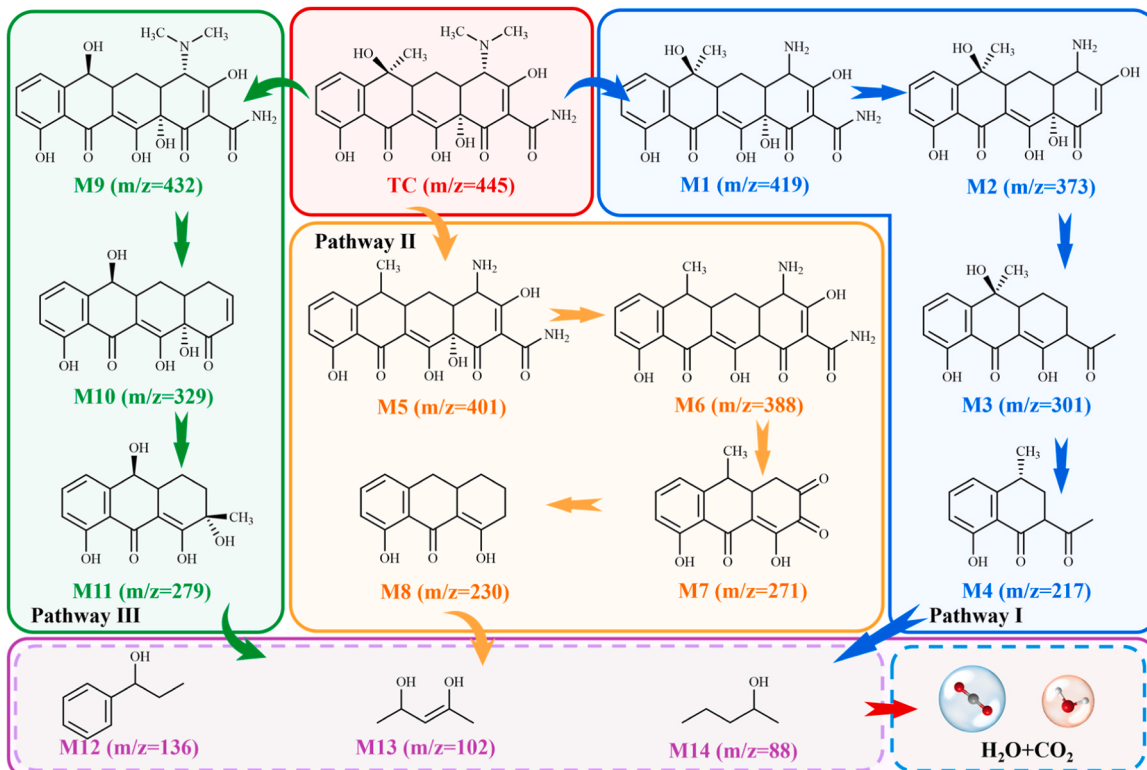


Fig. 14. Possible degradation pathways of TC in $\text{AgI}/\text{Cu-BiVO}_4/\text{PMS}/\text{Vis}$ system.

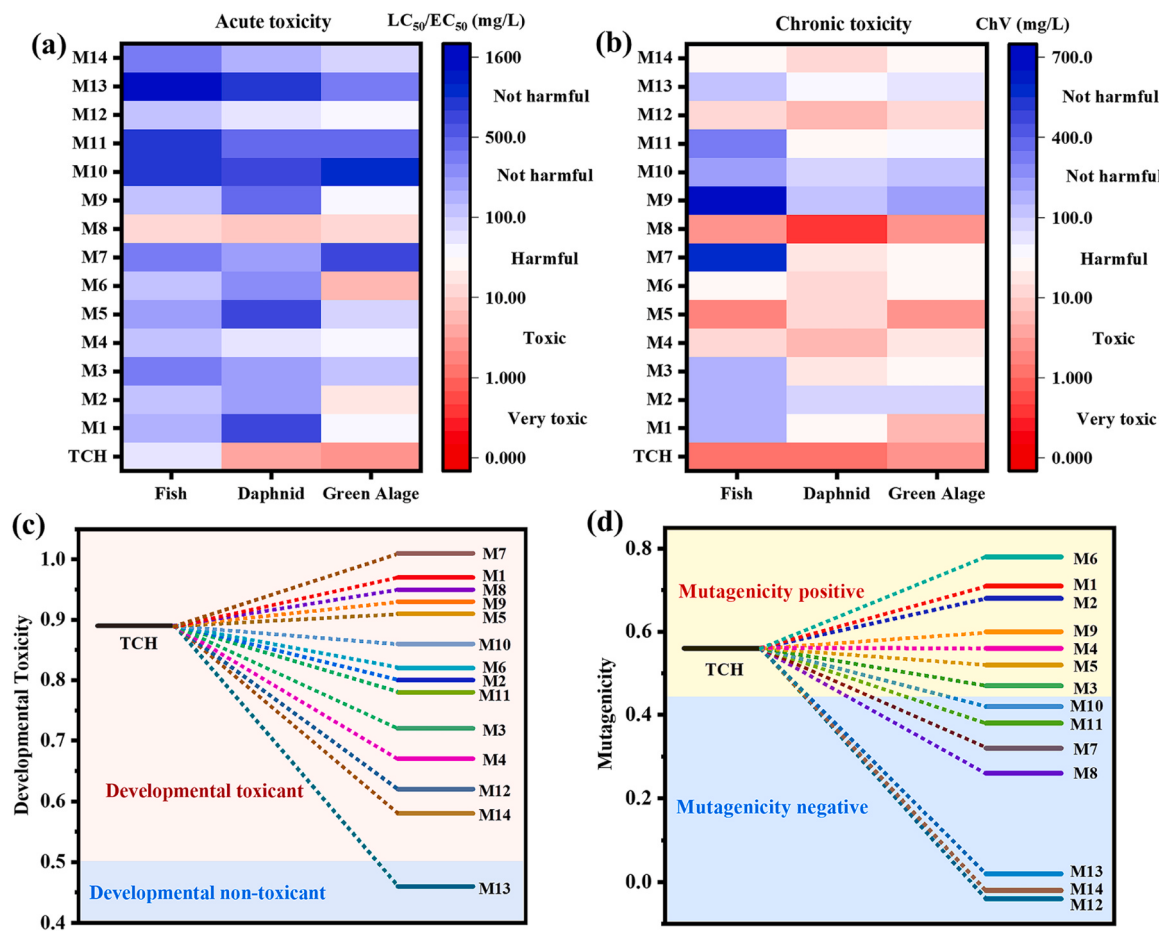


Fig. 15. . (a) acute toxicity, (b) chronic toxicity, (c) developmental toxicity and (d) mutagenicity of TC and its degradation intermediates.

3.5. Degradation pathways and toxicity assessment

To reveal the possible reaction sites and behavior of TC in the AgI/Cu-BiVO₄/PMS/Vis system under the radical or non-radical pathway, DFT calculations were performed on the TC molecule. The optimized molecular structure of TC is shown in Fig. 13a. The HOMO and LUMO of TC could elucidate the electron-rich and electron-poor regions, respectively (Fig. 13b-c). Apparently, the benzene ring, carbonyl and phenol group structures of TC tend to favor nucleophilic attack and exhibit electron-poor properties, while the electron-rich regions are mainly clustered in the dimethylamino group of TC [76]. To better predict the reaction trend of individual atoms on TC, their Fukui index (Table S10) and electrostatic potential (ESP) maps (Fig. 13d-f) were obtained based on Hirshfeld and npa charge analyses. Theoretically, higher values of f , f^+ and f^0 represent greater susceptibility to attacks by electrophilic groups ($^1\text{O}_2$ and h^+), nucleophilic groups ($\bullet\text{O}_2^-$) and general radicals ($\bullet\text{OH}$ and SO_4^{2-}), respectively [26]. The 13 C, 8 O, 17 C, and 9 N sites showed high f values, indicating greater vulnerability to $^1\text{O}_2$ and h^+ attacks during the reaction, while the 18 C, 3 O, and 22 C atoms with high f^+ values were more inclined to be attacked by $\bullet\text{O}_2^-$. In addition, 3 O, 6 O, 31 C and 18 C sites with high f^0 values are more susceptible to attack by $\bullet\text{OH}$ and SO_4^{2-} , thus facilitating the interfacial reaction. Interestingly, the corresponding isosurface maps (Fig. 13g-i) also visually validate the reaction behavior of atoms on the TC molecule.

The degradation intermediates of TC were identified by LC-MS (Fig. S21 and Table S11), and three possible degradation pathways were deduced based on DFT calculation (Fig. 14). In pathway I, TC ($m/z=445$) was attacked by $^1\text{O}_2$ and h^+ and undergoes demethylation to M1 ($m/z=419$) at 9 N ($f=0.029481$) position [83]. Then, the by-product M2 ($m/z=373$) was further formed by deamidation under attack by $\bullet\text{OH}$ and

SO_4^{2-} [77]. Apparently, M3 ($m/z=301$) and M4 ($m/z=217$) were formed by dehydroxylation and right-side opening epoxy reactions via $\bullet\text{O}_2^-$ and $\bullet\text{OH}$ attack. In pathway II, $\bullet\text{O}_2^-$, $^1\text{O}_2$ or h^+ attack the 16 C and 9 N sites of TC, resulting in dehydroxylation and N-demethylation to form the primary intermediate M5 ($m/z=401$) [84]. Then, M5 was dehydroxylated to M6 ($m/z=388$) intermediate under the action of $\bullet\text{OH}$. After a series of deamidation, dehydroxylation, ring opening and C=O bond-breaking reactions, M7 ($m/z=271$) and M8 ($m/z=230$) were produced [85]. In pathway III, the 25 C site of TC was susceptible to attack by $^1\text{O}_2$, h^+ , and free radicals and underwent demethylation and dehydroxylation to form M9 ($m/z=432$) [86]. M9 underwent N-demethylation, deamidation, and dehydroxylation to obtain M10 ($m/z=329$). Notably, M11 ($m/z=279$) was produced from M10 by methylation and attacked by $\bullet\text{O}_2^-$ and $\bullet\text{OH}$ in a ring-opening reaction and C=O bond breaking [87]. The intermediates M4, M8 and M11 were further degraded by ring-opening cleavage reaction to form small molecule intermediates such as M12 ($m/z=136$), M13 ($m/z=102$), and M14 ($m/z=88$), and finally completely mineralized into CO_2 and H_2O .

The toxicity evolution of TC and its intermediates was evaluated by using the ECOSAR software and the Toxicity Evaluation Software Tool (T.E.S.T) (Fig. 15 and Table S12). The heatmap results (Fig. 15a-b) showed that LC₅₀, EC₅₀ and ChV values were significantly elevated for most intermediates, and were eventually converted to the low toxicity M13-15. This indicated that the degradation of TC by this system could significantly reduce the ecotoxicity of the environment [26]. Interestingly, the reduction in acute toxicity of these intermediates was even more pronounced. Meanwhile, the reduction of chronic toxicity of fish and green algae was higher than that of daphnia. In addition, as shown in Fig. 15c-d, the developmental toxicity and mutagenicity of most of the intermediates decreased as the degradation process progressed. Among

them, the M13 intermediate was predicted to be developmental non-toxicity, and the M7–8 and M11–14 intermediates were also detected as mutagenicity negative. In summary, the AgI/Cu-BiVO₄/PMS/Vis system can efficiently achieve the removal of organic pollutants, while ensuring a green, safe and environmentally friendly degradation process.

4. Conclusions

In summary, the AgI/Cu-BiVO₄ S-scheme heterojunction with abundant oxygen defects was successfully prepared based on band modulation and defect engineering. This achieves dual modulation of photogenerated carrier separation kinetics and PMS activation sites, which greatly enhances the performance of PMS-activated photocatalysis for TC degradation and *M. aeruginosa* inactivation. The formation of ordered heterostructures and surface oxygen vacancies greatly accelerated the interfacial charge transfer and promoted the activation of PMS. The 0.25-ACBV/PMS/Vis system exhibited the optimal catalytic and PMS activation performance for mineralization of TC, with degradation rate constants 5.3 and 3.8 times higher than that of 0.25-ACBV/Vis and 0.25-ACBV/PMS, respectively. It also demonstrates excellent stability and general adaptability for different environmental conditions, including pH values (3–11), coexisting anions and HA, various pollutants (including dyes like MB and RhB, antibiotics like OTC and NOR), and real water matrices. Moreover, the rapid and effective inactivation of *M. aeruginosa* and oxidation of EOM confirms the outstanding advantage of the 0.25-ACBV heterojunction in controlling HABs in water bodies. The essence of the superior photocatalytic performance of AgI/Cu-BiVO₄-activated PMS was the S-scheme charge transfer mechanism driven by BIEF, which enhances the carrier transfer kinetics and maintains a high redox capacity. The synergistic effects of the Cu²⁺/Cu⁺ cycle and surface oxygen vacancies, acting as electron capture traps and activation sites, significantly promote the adsorption activation of PMS and the generation of ROS during the reaction process. In addition, the environmental friendliness of the system for pollutant degradation was determined by theoretical calculations and toxicological simulations. This study presents a theoretical basis and reference for the working mechanism of utilizing S-scheme heterojunction to drive PMS activation in photocatalytic coupling for environmental remediation.

CRediT authorship contribution statement

Zhuoya Li: Data curation. **Dong Wang:** Writing – review & editing, Supervision. **Yue Xuan:** Resources. **Liping Wang:** Writing – review & editing, Funding acquisition. **Jing Li:** Writing – original draft, Methodology, Investigation, Data curation, Conceptualization. **Dandan Wang:** Resources, Investigation. **Siyuan Zhao:** Software, Investigation. **Rui Ma:** Methodology, Investigation. **Jifeng Guo:** Writing – review & editing, Supervision, Investigation, Funding acquisition.

Declaration of Competing Interest

The authors declare that they have no known competing financial interests or personal relationships that could have appeared to influence the work reported in this paper.

Data Availability

Data will be made available on request.

Acknowledgments

This work was supported by the National Natural Science Foundation of China (52300217), the China National Key R&D Program (2021YFE0192600), the Scientific Research Program Funded by Shaanxi Provincial Education Department (22JE008), the Fundamental Research

Funds for the Central Universities, CHD (300102292903, 300102293727), and the Students'Innovation and Entrepreneurship Training Plan by CHD (S202310710227). The scientific calculations in this paper have been done on the HPC Cloud Platform of Shandong University.

Appendix A. Supporting information

Supplementary data associated with this article can be found in the online version at doi:10.1016/j.apcatb.2024.124007.

References

- [1] Y. Lin, C. Yang, Q. Niu, S. Luo, Interfacial charge transfer between silver phosphate and W₂N₃ induced by nitrogen vacancies enhances removal of β -Lactam antibiotics, Adv. Funct. Mater. 32 (2022) 2108814, <https://doi.org/10.1002/adfm.202108814>.
- [2] C. Hu, J. Cao, X. Jia, H. Sun, H. Lin, S. Chen, Difunctional Ni₂P decorated novel Z-scheme BiVO₄/g-C₃N₄ heterojunction for achieving highly efficient CO₂ reduction and tetracycline oxidation, Appl. Catal. B: Environ. 337 (2023) 122957, <https://doi.org/10.1016/j.apcatb.2023.122957>.
- [3] S. Li, C. Wang, Y. Liu, M. Cai, Y. Wang, H. Zhang, Y. Guo, W. Zhao, Z. Wang, X. Chen, Photocatalytic degradation of tetracycline antibiotic by a novel Bi₂Sn₂O₇/Bi₂MoO₆ S-scheme heterojunction: Performance, mechanism insight and toxicity assessment, Chem. Eng. J. 429 (2022) 132519, <https://doi.org/10.1016/j.cej.2021.132519>.
- [4] G. Fan, X. Li, J. Lin, X. Wu, L. Zhang, J. Wu, Y. Wang, Efficient photocatalytic inactivation of *Microcystis aeruginosa* via self-floating Ag₃VO₄/BiVO₄ hydrogel under visible light, Sep. Purif. Technol. 299 (2022) 121803, <https://doi.org/10.1016/j.seppur.2022.121803>.
- [5] S. Sun, Q. Tang, H. Xu, Y. Gao, W. Zhang, L. Zhou, Y. Li, J. Wang, C. Song, A comprehensive review on the photocatalytic inactivation of *Microcystis aeruginosa*: performance, development, and mechanisms, Chemosphere 312 (2023) 137239, <https://doi.org/10.1016/j.chemosphere.2022.137239>.
- [6] R.G. Maset, A. Hapeshi, J. Lapage, N. Harrington, J. Littler, S. Perrier, F. Harrison, Combining SNAPs with antibiotics shows enhanced synergistic efficacy against *S. aureus* and *P. aeruginosa* biofilms, npj Biofilms Micro 9 (2023) 36, <https://doi.org/10.1038/s41522-023-00401-8>.
- [7] Y. Jiang, Y. Liu, J. Zhang, Mechanisms for the stimulatory effects of a five-component mixture of antibiotics in *Microcystis aeruginosa* at transcriptomic and proteomic levels, J. Hazard. Mater. 406 (2021) 124722, <https://doi.org/10.1016/j.jhazmat.2020.124722>.
- [8] L. Zhou, X. Zhang, M. Cai, N. Cui, G. Chen, G. Zou, New insights into the efficient charge transfer of the modified-TiO₂/Ag₃PO₄ composite for enhanced photocatalytic destruction of algal cells under visible light, Appl. Catal. B: Environ. 302 (2022) 120868, <https://doi.org/10.1016/j.apcatb.2021.120868>.
- [9] C. Wu, J. Dai, J. Ma, T. Zhang, L. Qiang, J. Xue, Mechanistic study of B-TiO₂/BiVO₄ S-scheme heterojunction photocatalyst for tetracycline hydrochloride removal and H₂ production, Sep. Purif. Technol. 312 (2023) 123398, <https://doi.org/10.1016/j.seppur.2023.123398>.
- [10] C. Hou, Y. Li, M. Niu, Y. Liu, X. Kong, M. Zhang, L. Wang, Construction of an all-solid-state Z-scheme Ag@Ag₃PO₄/TiO₂-(F2) heterostructure with enhanced photocatalytic activity, photocorrosion resistance and mechanism insight, J. Alloy. Compd. 925 (2022) 166765, <https://doi.org/10.1016/j.jallcom.2022.166765>.
- [11] H. Li, H. Gong, Z. Jin, Phosphorus modified Ni-MOF-74/BiVO₄ S-scheme heterojunction for enhanced photocatalytic hydrogen evolution, Appl. Catal. B: Environ. 307 (2022) 121166, <https://doi.org/10.1016/j.apcatb.2022.121166>.
- [12] J. Kang, Y. Tang, M. Wang, C. Jin, J. Liu, S. Li, Z. Li, J. Zhu, The enhanced peroxymonosulfate-assisted photocatalytic degradation of tetracycline under visible light by g-C₃N₄/Na-BiVO₄ heterojunction catalyst and its mechanism, J. Environ. Chem. Eng. 9 (2021) 105524, <https://doi.org/10.1016/j.jeche.2021.105524>.
- [13] X. Zheng, X. Zhang, Y. Cai, S. Zhao, S. Wang, Efficient degradation of bisphenol A with MoS₂/BiVO₄ hetero-nanoflower as a heterogenous peroxymonosulfate activator under visible-light irradiation, Chemosphere 289 (2022) 133158, <https://doi.org/10.1016/j.chemosphere.2021.133158>.
- [14] X. Yue, L. Cheng, J. Fan, Q. Xiang, 2D/2D BiVO₄/CsPbBr₃ S-scheme heterojunction for photocatalytic CO₂ reduction: Insights into structure regulation and Fermi level modulation, Appl. Catal. B: Environ. 304 (2022) 120979, <https://doi.org/10.1016/j.apcatb.2021.120979>.
- [15] Y. He, J. Qian, P. Wang, T. Xie, D.D. Dionysiou, B. Lu, S. Tang, Synergized selenium-vacancy heterogeneous interface and carbon nanotubes for insight into efficient oxidation of pollutants via photocatalytic peroxymonosulfate activation, Appl. Catal. B: Environ. 330 (2023) 122620, <https://doi.org/10.1016/j.apcatb.2023.122620>.
- [16] L. Zhang, J. Zhang, H. Yu, J. Yu, Emerging S-Scheme Photocatalyst, Adv. Mater. 34 (2022), <https://doi.org/10.1002/adma.202107668>.
- [17] Y. Yuan, W.G. Pan, R.T. Guo, L.F. Hong, Z.D. Lin, X.Y. Ji, Flower spherical-like Bi₇O₉I₃/AgI S-scheme heterojunction for phenol photodegradation: the synergistic effect of dual surface plasmon resonance and photothermal property, Sep. Purif. Technol. 297 (2022) 121538, <https://doi.org/10.1016/j.seppur.2022.121538>.

[18] Z. Chen, Y. Li, F. Tian, X. Chen, Z. Wu, Synthesis of BiVO₄/g-C₃N₄ S-scheme heterojunction via a rapid and green microwave route for efficient removal of glyphosate, *Sep. Purif. Technol.* 287 (2022) 120507, <https://doi.org/10.1016/j.seppur.2022.120507>.

[19] Y. Dong, X. Wang, H. Sun, H. Zhang, X. Zhao, L. Wang, Construction of a 0D/3D AgI/MOF-808 photocatalyst with a one-photon excitation pathway for enhancing the degradation of tetracycline hydrochloride: mechanism, degradation pathway and DFT calculations, *Chem. Eng. J.* 460 (2023) 141842, <https://doi.org/10.1016/j.cej.2023.141842>.

[20] S. Sun, Q. Tang, T. Yu, Y. Gao, W. Zhang, L. Zhou, H. Elhelgazy, K. He, Fabrication of g-C₃N₄@Bi₂MoO₆@AgI floating sponge for photocatalytic inactivation of Microcystis aeruginosa under visible light, *Environ. Res.* 215 (2022) 114216, <https://doi.org/10.1016/j.envres.2022.114216>.

[21] F. Liu, C. Nie, Q. Dong, Z. Ma, W. Liu, M. Tong, AgI modified covalent organic frameworks for effective bacterial disinfection and organic pollutant degradation under visible light irradiation, *J. Hazard. Mater.* 398 (2020) 122865, <https://doi.org/10.1016/j.jhazmat.2020.122865>.

[22] W. Zhao, J. Li, B. Dai, Z. Cheng, J. Xu, K. Ma, L. Zhang, N. Sheng, G. Mao, H. Wu, K. Wei, D.Y.C. Leung, Simultaneous removal of tetracycline and Cr(VI) by a novel three-dimensional AgI/BiVO₄ p-n junction photocatalyst and insight into the photocatalytic mechanism, *Chem. Eng. J.* 369 (2019) 716–725, <https://doi.org/10.1016/j.cej.2019.03.115>.

[23] P. Ju, L. Hao, Y. Zhang, J. Sun, K. Dou, Z. Lu, D. Liao, X. Zhai, C. Sun, Facile fabrication of a novel spindlelike MoS₂/BiVO₄ Z-scheme heterostructure with superior visible-light-driven photocatalytic disinfection performance, *Sep. Purif. Technol.* 299 (2022) 121706, <https://doi.org/10.1016/j.seppur.2022.121706>.

[24] G. Chen, Y. Yu, L. Liang, X. Duan, R. Li, X. Lu, B. Yan, N. Li, S. Wang, Remediation of antibiotic wastewater by coupled photocatalytic and persulfate oxidation system: a critical review, *J. Hazard. Mater.* 408 (2021) 124461, <https://doi.org/10.1016/j.jhazmat.2020.124461>.

[25] Y. Deng, J. Wang, J. Wang, H. Zhang, H. Xiao, C. Zhang, W. Wang, In situ growth of Bi/Ag double quantum dots on hollow Bi₂MoO₆ microspheres: Enhancement of the surface plasmon resonance effect on PMS activation, *Appl. Catal. B: Environ.* 338 (2023) 123041, <https://doi.org/10.1016/j.apcatb.2023.123041>.

[26] R. Tang, H. Zeng, Y. Deng, S. Xiong, L. Li, Z. Zhou, J. Wang, L. Tang, Dual modulation on peroxymonosulfate activation site and photocarrier separation in carbon nitride for efficient photocatalytic organics degradation: efficacy and mechanism evaluation, *Appl. Catal. B: Environ.* 336 (2023) 122918, <https://doi.org/10.1016/j.apcatb.2023.122918>.

[27] X. Zhang, Z. Chen, X. Li, Y. Wu, J. Zheng, Y. Li, D. Wang, Q. Yang, A. Duan, Y. Fan, Promoted electron transfer in Fe²⁺/Fe³⁺ co-doped BiVO₄/Ag₃Po₄ S-scheme heterojunction for efficient photo-Fenton oxidation of antibiotics, *Sep. Purif. Technol.* 310 (2023) 123116, <https://doi.org/10.1016/j.seppur.2023.123116>.

[28] S. Zhang, X. Ou, X. Yang, D. Wang, C. Zhang, Preparation and properties of Al³⁺-doped BiVO₄ semiconductor photocatalyst, *Chem. Phys. Lett.* 778 (2021) 138747, <https://doi.org/10.1016/j.cplett.2021.138747>.

[29] C. Regmi, Y.K. Kshetri, R.P. Pandey, T.-H. Kim, G. Gyawali, S.W. Lee, Understanding the multifunctionality in Cu-doped BiVO₄ semiconductor photocatalyst, *J. Environ. Sci.* 75 (2019) 84–97, <https://doi.org/10.1016/j.jes.2018.03.005>.

[30] X. Hu, J. Wang, J. Wang, Y. Deng, H. Zhang, T. Xu, W. Wang, β particles induced directional inward migration of oxygen vacancies: Surface oxygen vacancies and interface oxygen vacancies synergistically activate PMS, *Appl. Catal. B: Environ.* 318 (2022) 121879, <https://doi.org/10.1016/j.apcatb.2022.121879>.

[31] Y. Tian, D. Que, R. Guan, W. Shi, SiO₂ template-modified and Cu-doped BiVO₄ with high visible-light photocatalytic performance: Preparation and first-principles study, *Mater. Today Commun.* 32 (2022) 103954, <https://doi.org/10.1016/j.mtcomm.2022.103954>.

[32] X. Dou, Y. Chen, H. Shi, CuBi₂O₄/BiOBr composites promoted PMS activation for the degradation of tetracycline: S-scheme mechanism boosted Cu²⁺/Cu⁺ cycle, *Chem. Eng. J.* 431 (2022) 134054, <https://doi.org/10.1016/j.cej.2021.134054>.

[33] Y. Li, Z. Wang, C. Li, F. Qi, P. Yan, Y. Wang, M. He, Z. Chen, Q. Wang, Y. Wang, H. Zheng, A. Ikhlaq, J. Kumirska, E. Maria Siedlecka, O. Ismailova, Reducing agents enhanced prometron degradation by CuBi₂O₄/peroxymonosulfate: Development of interfacial electron transport and circulation of Cu⁺/Cu²⁺, *Chem. Eng. J.* 470 (2023) 144387 <https://doi.org/10.1016/j.cej.2023.144387>.

[34] Z. Long, H. Wang, K. Huang, G. Zhang, H. Xie, Di-functional Cu²⁺-doped BiOCl photocatalyst for degradation of organic pollutant and inhibition of cyanobacterial growth, *J. Hazard. Mater.* 424 (2022) 127554, <https://doi.org/10.1016/j.jhazmat.2021.127554>.

[35] J. Zhao, F. Ning, X. Cao, H. Yao, Z. Wang, B. Xing, Photo-transformation of graphene oxide in the presence of co-existing metal ions regulated its toxicity to freshwater algae, *Water Res* 176 (2020) 115735, <https://doi.org/10.1016/j.watres.2020.115735>.

[36] R. Acosta-Herazo, M.Á. Mueses, G.L. Puma, F. Machuca-Martínez, Impact of photocatalyst optical properties on the efficiency of solar photocatalytic reactors rationalized by the concepts of initial rate of photon absorption (IRPA) dimensionless boundary layer of photon absorption and apparent optical thickness, *Chem. Eng. J.* 356 (2019) 839–849, <https://doi.org/10.1016/j.cej.2018.09.085>.

[37] D. Wang, M.A. Mueses, J.A.C. Márquez, F. Machuca-Martínez, I. Grčić, R. Peralta Muniz Moreira, G. Li Puma, Engineering and modeling perspectives on photocatalytic reactors for water treatment, *Water Res* 202 (2021) 117421, <https://doi.org/10.1016/j.watres.2021.117421>.

[38] I. Grčić, G. Li Puma, Six-flux absorption-scattering models for photocatalysis under wide-spectrum irradiation sources in annular and flat reactors using catalysts with different optical properties, *Appl. Catal. B: Environ.* 211 (2017) 222–234, <https://doi.org/10.1016/j.apcatb.2017.04.014>.

[39] L. Hurtado, R. Natividad, E. Torres-García, J. Farias, G. Li Puma, Correlating the photocatalytic activity and the optical properties of Li₂MoO₆ photocatalyst under the UV and the visible region of the solar radiation spectrum, *Chem. Eng. J.* 262 (2015) 1284–1291, <https://doi.org/10.1016/j.cej.2014.10.052>.

[40] I. Grčić, G. Li Puma, Photocatalytic degradation of water contaminants in multiple photoreactors and evaluation of reaction kinetic constants independent of photon absorption, irradiance, reactor geometry, and hydrodynamics, *Environ. Sci. Technol.* 47 (2013) 13702–13711, <https://doi.org/10.1021/es403472e>.

[41] R. Acosta-Herazo, J. Monterroza-Romero, M.Á. Mueses, F. Machuca-Martínez, G. Li Puma, Coupling the Six Flux Absorption-Scattering Model to the Henyey-Greenstein scattering phase function: Evaluation and optimization of radiation absorption in solar heterogeneous photoreactors, *Chem. Eng. J.* 302 (2016) 86–96, <https://doi.org/10.1016/j.cej.2016.04.127>.

[42] R. Peralta Muniz Moreira, G. Li Puma, Multiphysics Computational Fluid-Dynamics (CFD) Modeling of Annular Photocatalytic Reactors by the Discrete Ordinates Method (DOM) and the Six-Flux Model (SFM) and evaluation of the contaminant intrinsic kinetics constants, *Catal. Today* 361 (2021) 77–84, <https://doi.org/10.1016/j.cattod.2020.01.012>.

[43] G. Kresse, J. Furthmüller, Efficiency of ab-initio total energy calculations for metals and semiconductors using a plane-wave basis set, *Comp. Mater. Sci.* 6 (1996) 15–50, [https://doi.org/10.1016/0927-0256\(96\)00008-0](https://doi.org/10.1016/0927-0256(96)00008-0).

[44] P.P. John, B. Kierow, E. Matthias, Generalized gradient approximation made simple, *Phys. Rev. Lett.* (1996), <https://doi.org/10.1103/PhysRevLett.77.3865>.

[45] S. Ma, D. Chen, Y. Zhong, Y. Feng, Z. He, W. Zhang, Y. Zhang, H. Ding, X. Wu, Oxygen vacancy simultaneously inducing peroxymonosulfate activation and photocatalytic reaction for highly efficient ciprofloxacin degradation, *Chem. Eng. J.* 467 (2023) 143385, <https://doi.org/10.1016/j.cej.2023.143385>.

[46] M. Frisch, G.W. Trucks, H.B. Schlegel, G.E. Scuseria, M.A. Robb, J.R. Cheeseman, G. Scalmani, V. Barone, B. Mennucci, G. Petersson, Gaussian 09, revision D.01, Gaussian, Inc., Wallingford CT, 2009.

[47] T. Lu, F. Chen, Multiwfns: a multifunctional wavefunction analyzer, *J. Comput. Chem.* (2012), <https://doi.org/10.1002/jcc.22885>.

[48] S.K. Lakhera, R. Venkataramana, G. Mathew, H.Y. Hafeez, B. Neppolian, Fabrication of high surface area AgI incorporated porous BiVO₄ heterojunction photocatalysts, *Mat. Sci. Semicon. Proc.* 106 (2020) 104756, <https://doi.org/10.1016/j.msspc.2019.104756>.

[49] S. Moscow, V. Kavinkumar, M. Sriramkumar, K. Jothivenkatachalam, P. Saravanan, N. Rajamohan, Y. Vasheghian, M. Rajasimman, Impact of Erbium (Er) and Yttrium (Y) doping on BiVO₄ crystal structure towards the enhancement of photoelectrochemical water splitting and photocatalytic performance, *Chemosphere* 299 (2022) 134343, <https://doi.org/10.1016/j.chemosphere.2022.134343>.

[50] H. Huang, Y. Li, H. Wang, W. Jiang, In situ fabrication of ultrathin-g-C₃N₄/AgI heterojunctions with improved catalytic performance for photodegrading rhodamine B solution, *Appl. Surf. Sci.* 538 (2021) 148132, <https://doi.org/10.1016/j.apsusc.2020.148132>.

[51] M. Mousavi-Kamazani, Cube-like Cu/Cu₂O/Bi₂VO₁₃ composite nanoparticles: Facile sol-gel synthesis for photocatalytic desulfurization of thiophene under visible light, *J. Alloy. Compd.* 823 (2020) 153786, <https://doi.org/10.1016/j.jallcom.2020.153786>.

[52] J. Chen, H. Zhu, Q. Ren, S. Chen, Y. Ding, Z. Jin, C. Xiong, W. Guo, X. Jia, Efficient degradation of atrazine residues in wastewater by persulfate assisted Ag₃VO₄/Bi₂MoO₆/diatomite under visible light, *J. Environ. Chem. Eng.* 10 (2022) 107938, <https://doi.org/10.1016/j.je.2022.107938>.

[53] T. Sharifi, D. Crmaric, M. Kovacic, M. Popovic, M.K. Rokovic, H. Kusic, D. Jozic, G. Ambrožić, D. Kralj, J. Kontrec, B. Zener, U.L. Stangar, D.D. Dionysiou, A. L. Bozic, Tailored BiVO₄ for enhanced visible-light photocatalytic performance, *J. Environ. Chem. Eng.* 9 (2021) 106025, <https://doi.org/10.1016/j.je.2021.106025>.

[54] Z. Zhou, L. Zhang, W. Su, Y. Li, G. Zhang, Facile fabrication of AgI/Sb₂O₃ heterojunction photocatalyst with enhanced visible-light driven photocatalytic performance for efficient degradation of organic pollutants in water, *Environ. Res.* 197 (2021) 111143, <https://doi.org/10.1016/j.envres.2021.111143>.

[55] H. Fang, Y. Han, X. Feng, W. Ji, C.-T. Au, S-scheme heterojunction g-C₃N₄/Ag/Ag₂CO for efficient tetracycline removal in a photo-assisted peroxymonosulfate system, *Sep. Purif. Technol.* 296 (2022) 121210, <https://doi.org/10.1016/j.seppur.2022.121210>.

[56] L. Wang, Y. Xue, G. Yang, X. Liu, W. He, M. Zhang, Z. Liu, Electronic structure regulation of an S-scheme CuBi₂O₄/Sr_{0.5}NaTaO₃ heterojunction with efficient carrier spatial transfer, *Sep. Purif. Technol.* 317 (2023), <https://doi.org/10.1016/j.seppur.2023.123856>.

[57] X. Li, T. Chen, Y. Qiu, Z. Zhu, H. Zhang, D. Yin, Magnetic dual Z-scheme g-C₃N₄/BiVO₄/CuFe₂O₄ heterojunction as an efficient visible-light-driven peroxymonosulfate activator for levofloxacin degradation, *Chem. Eng. J.* 452 (2023) 139659, <https://doi.org/10.1016/j.cej.2022.139659>.

[58] S.K. Lakhera, H.Y. Hafeez, R. Venkataramana, P. Veluswamy, H. Choi, B. Neppolian, Design of a highly efficient ternary AgI/rGO/BiVO₄ nanocomposite and its direct solar light induced photocatalytic activity, *Appl. Surf. Sci.* 487 (2019) 1289–1300, <https://doi.org/10.1016/j.apsusc.2019.05.201>.

[59] K. Manikantan, K. Shanmugasundaram, P. Thirunavukkarasu, Enhanced photocatalytic dye degradation and hydrogen evolution performance of Cu encapsulated BiVO₄ under visible light irradiation, *Chem. Phys. Impact* 6 (2023) 100178, <https://doi.org/10.1016/j.chphi.2023.100178>.

[60] Z. Chen, N. Mi, L. Huang, W. Wang, C. Li, Y. Teng, C. Gu, Snow-like BiVO₄ with rich oxygen defects for efficient visible light photocatalytic degradation of ciprofloxacin, *Sci. Total Environ.* 808 (2022) 152083, <https://doi.org/10.1016/j.scitotenv.2021.152083>.

[61] H.L. Tan, A. Suyanto, A.T.D. Denko, W.H. Saputera, R. Amal, F.E. Osterloh, Y. H. Ng, Enhancing the Photoactivity of Faceted BiVO₄ via Annealing in Oxygen-Deficient Condition, Part. Part. Syst. Charact. 34 (2017) 1600290, <https://doi.org/10.1002/ppsc.201600290>.

[62] S. Ning, H. Lin, Y. Tong, X. Zhang, Q. Lin, Y. Zhang, J. Long, X. Wang, Dual couples Bi metal depositing and Ag@AgI islanding on BiOI 3D architectures for synergistic bactericidal mechanism of *E. coli* under visible light, *Appl. Catal. B: Environ.* 204 (2017) 1–10, <https://doi.org/10.1016/j.apcatb.2016.11.006>.

[63] J. Liang, C. Shan, X. Zhang, M. Tong, Bactericidal mechanism of BiOI-AgI under visible light irradiation, *Chem. Eng. J.* 279 (2015) 277–285, <https://doi.org/10.1016/j.cej.2015.05.024>.

[64] M. Zhang, Y. Li, B. Yang, Y. Su, J. Xu, J. Deng, T. Zhou, Promoted BPA degradation in food waste leachate via alkali-fluffed CoFe₂O₄@CoSiO_x activated PMS under the assistance of inherent acetate, *Sep. Purif. Technol.* 306 (2023) 122566, <https://doi.org/10.1016/j.seppur.2022.122566>.

[65] K. Zhu, W. Qin, Y. Gan, Y. Huang, Z. Jiang, Y. Chen, X. Li, K. Yan, Acceleration of Fe³⁺/Fe²⁺ cycle in garland-like MIL-101(Fe)/MoS₂ nanosheets to promote peroxymonosulfate activation for sulfamethoxazole degradation, *Chem. Eng. J.* 470 (2023) 144190, <https://doi.org/10.1016/j.cej.2023.144190>.

[66] X. Chen, Y. Chen, S. Li, C. Xue, D. Liu, W. Huang, Unraveling the crucial role of Mo₂N from Fe/Mo bimetal MOF-derived catalyst in initiating Fe³⁺/Fe²⁺ redox cycle to activate peroxymonosulfate for dibutyl phthalate degradation, *Chem. Eng. J.* 476 (2023) 146693, <https://doi.org/10.1016/j.cej.2023.146693>.

[67] H. Zhang, Y. He, M. He, Q. Yang, G. Ding, Y. Mo, Z. Liu, P. Gao, Construction of cubic CaTiO₃ perovskite modified by highly-dispersed cobalt for efficient catalytic degradation of psychoactive pharmaceuticals, *J. Hazard. Mater.* 459 (2023) 132191, <https://doi.org/10.1016/j.jhazmat.2023.132191>.

[68] C. Xiao, Y. Hu, Q. Li, J. Liu, X. Li, Y. Shi, Y. Chen, J. Cheng, Carbon-doped defect MoS₂ co-catalytic Fe³⁺/peroxymonosulfate process for efficient sulfadiazine degradation: Accelerating Fe³⁺/Fe²⁺ cycle and O₂ dominated oxidation, *Sci. Total Environ.* 858 (2023) 159587, <https://doi.org/10.1016/j.scitotenv.2022.159587>.

[69] J. Yan, H. Liu, C. Dou, Y. Wu, W. Dong, Quantitative probing of reactive oxygen species and their selective degradation on contaminants in peroxymonosulfate-based process enhanced by picolinic acid, *J. Hazard. Mater.* 459 (2023) 132083, <https://doi.org/10.1016/j.jhazmat.2023.132083>.

[70] X. Chen, L. Yao, J. He, J. Li, S. Xu, N. Li, Y. Zhu, X. Chen, R. Zhu, Enhanced degradation of tetracycline under natural sunlight through the synergistic effect of Ag₃PO₄/MIL-101(Fe) photocatalysis and Fenton catalysis: Mechanism, pathway, and toxicity assessment, *J. Hazard. Mater.* 449 (2023) 131024, <https://doi.org/10.1016/j.jhazmat.2023.131024>.

[71] Y. Wen, Z. Wang, Y. Cai, M. Song, K. Qi, X. Xie, S-scheme BiVO₄/CQDs/β-FeOOH photocatalyst for efficient degradation of ofloxacin: Reactive oxygen species transformation mechanism insight, *Chemosphere* 295 (2022) 133784, <https://doi.org/10.1016/j.chemosphere.2022.133784>.

[72] Z. Wang, L. Jiang, K. Wang, Y. Li, G. Zhang, Novel AgI/BiSbO₄ heterojunction for efficient photocatalytic degradation of organic pollutants under visible light: interfacial electron transfer pathway, DFT calculation and degradation mechanism study, *J. Hazard. Mater.* 410 (2021) 124948, <https://doi.org/10.1016/j.jhazmat.2020.124948>.

[73] L. Xia, K. Zhang, X. Wang, Q. Guo, Y. Wu, Y. Du, L. Zhang, J. Xia, H. Tang, X. Zhang, Y. Peng, Z. Li, X. Yang, 0D/2D Schottky junction synergies with 2D/2D S-scheme heterojunction strategy to achieve uniform separation of carriers in 0D/2D/2D quasi CNQDs/TCN/ZnIn₂S₄ towards photocatalytic remediating petroleum hydrocarbons polluted marine, *Appl. Catal. B: Environ.* 325 (2023) 122387, <https://doi.org/10.1016/j.apcatb.2023.122387>.

[74] Y. Yuan, W. Pan, R. Guo, L. Hong, Z. Lin, X. Ji, Flower spherical-like Bi₂O₉I₃/AgI S-scheme heterojunction for phenol photodegradation: The synergistic effect of dual surface plasmon resonance and photothermal property, *Sep. Purif. Technol.* 297 (2022) 121538, <https://doi.org/10.1016/j.seppur.2022.121538>.

[75] J. Liu, G. Wang, B. Li, X. Ma, Y. Hu, H. Cheng, A high-efficiency mediator-free Z-scheme Bi₂MoO₆/AgI heterojunction with enhanced photocatalytic performance, *Sci. Total Environ.* 784 (2021) 147227, <https://doi.org/10.1016/j.scitotenv.2021.147227>.

[76] X. Zou, C. Li, L. Wang, W. Wang, J. Bian, H. Bai, X. Meng, Enhanced visible-light photocatalytic degradation of tetracycline antibiotic by 0D/2D TiO₂(B)/BiOCl Z-scheme heterojunction: Performance, reaction pathways, and mechanism investigation, *Appl. Surf. Sci.* 630 (2023) 157532, <https://doi.org/10.1016/j.apsusc.2023.157532>.

[77] H. Ren, F. Qi, A. Labidi, J. Zhao, H. Wang, Y. Xin, J. Luo, C. Wang, Chemically bonded carbon quantum dots/Bi₂WO₆ S-scheme heterojunction for boosted photocatalytic antibiotic degradation: Interfacial engineering and mechanism insight, *Appl. Catal. B: Environ.* 330 (2023) 122587, <https://doi.org/10.1016/j.apcatb.2023.122587>.

[78] Y. Sun, W. Han, F. Zhang, H. Li, Z. Zhang, X. Zhang, B. Shen, S.-Q. Guo, T. Ma, Dual defect regulation of BiOCl halogen layer enables photocatalytic O₂ activation into singlet oxygen for refractory aromatic pollutant removal, *Appl. Catal. B: Environ. Energy* 345 (2024) 123689, <https://doi.org/10.1016/j.apcatb.2023.123689>.

[79] J. Hu, F. Chen, K. Mu, J. Zhang, J. Lu, Enhanced photocatalytic O₂ activation by the synergy of efficient oxygen adsorption and interfacial charge separation: A case of Bi₂O₃Br/rGO van der Waals heterojunction, *Sep. Purif. Technol.* 286 (2022) 120416, <https://doi.org/10.1016/j.seppur.2021.120416>.

[80] P. Cai, J. Zhao, X. Zhang, T. Zhang, G. Yin, S. Chen, C.-L. Dong, Y.-C. Huang, Y. Sun, D. Yang, B. Xing, Synergy between cobalt and nickel on NiCo₂O₄ nanosheets promotes peroxymonosulfate activation for efficient norfloxacin degradation, *Appl. Catal. B: Environ.* 306 (2022) 121091, <https://doi.org/10.1016/j.apcatb.2022.121091>.

[81] Y. Shi, J. Li, D. Wan, J. Huang, Y. Liu, Peroxymonosulfate-enhanced photocatalysis by carbonyl-modified g-C₃N₄ for effective degradation of the tetracycline hydrochloride, *Sci. Total Environ.* 749 (2020) 142313, <https://doi.org/10.1016/j.scitotenv.2020.142313>.

[82] W. Zhang, L. Yan, Q. Wang, X. Li, Y. Guo, W. Song, Y. Li, Ball milling boosted the activation of peroxymonosulfate by biochar for tetracycline removal, *J. Environ. Chem. Eng.* 9 (2021) 106870, <https://doi.org/10.1016/j.jece.2021.106870>.

[83] Y. Liu, S. Liu, M. Chen, Y. Bai, Y. Liu, J. Mei, B. Lai, Enhanced TC degradation by persulfate activation with carbon-coated CuFe₂O₄: The radical and non-radical co-dominant mechanism, DFT calculations and toxicity evaluation, *J. Hazard. Mater.* 461 (2024) 132417, <https://doi.org/10.1016/j.jhazmat.2023.132417>.

[84] L. Su, P. Wang, M. Li, Z. Zhao, Y. Li, S. Zhan, Synergistic enhancement of photocatalytic molecular oxygen activation by nitrogen defect and interfacial photoelectron transfer over Z-scheme α-Fe₂O₃/g-C₃N₄ heterojunction, *Appl. Catal. B: Environ.* 335 (2023) 122890, <https://doi.org/10.1016/j.apcatb.2023.122890>.

[85] X. Wang, J. Jiang, Y. Ma, Y. Song, T. Li, S. Dong, Tetracycline hydrochloride degradation over manganese cobaltate (MnCo₂O₄) modified ultrathin graphitic carbon nitride (g-C₃N₄) nanosheet through the highly efficient activation of peroxymonosulfate under visible light irradiation, *J. Colloid Interf. Sci.* 600 (2021) 449–462, <https://doi.org/10.1016/j.jcis.2021.05.044>.

[86] M. Zhu, Y. Tang, X. Chen, B. Liao, Y. Yu, S. Hou, X. Fan, Internal electric field and oxygen vacancies synergistically optimized Ba²⁺ doped SrBi₂Bi₂O₇ for photocatalytic tetracycline degradation from water, *Chem. Eng. J.* 433 (2022) 134580, <https://doi.org/10.1016/j.cej.2022.134580>.

[87] X. Huang, X. Zhang, K. Zhang, X. Xue, J. Xiong, Y. Huang, D. Zhang, J. Zhang, Z. Zhang, F. Yan, Defect-mediated Z-scheme carriers' dynamics of C-ZnO/A-CN toward highly enhanced photocatalytic TC degradation, *J. Alloy. Compd.* 877 (2021) 160321, <https://doi.org/10.1016/j.jallcom.2021.160321>.